



Testing stomatal models at stand level in deciduous angiosperm and evergreen gymnosperm forests using CliMA Land (v0.1)

Yujie Wang¹, Philipp Köhler¹, Liyin He¹, Russell Doughty¹, Renato K. Braghieri^{2,3}, Jeffrey D. Wood⁴, and Christian Frankenberg¹

¹Division of Geological and Planetary Sciences, California Institute of Technology, Pasadena, California 91125, USA

²Jet Propulsion Laboratory, California Institute of Technology, Pasadena, California 91109, USA

³Joint Institute for Regional Earth System Science and Engineering, University of California at Los Angeles, Los Angeles, California 90095, USA

⁴School of Natural Resources, University of Missouri, Columbia, Missouri 65211, USA

Correspondence: Yujie Wang (wyujie@caltech.edu), Christian Frankenberg (cfranken@caltech.edu)

Abstract. At the leaf level, stomata control the exchange of water and carbon across the air-leaf interface. Stomatal conductance is typically modeled empirically, based on environmental conditions at the leaf surface. Recently developed stomatal optimization models show great skills at predicting carbon and water fluxes at both the leaf and tree levels. However, it has not been evaluated how well the optimization models perform at larger scales. Furthermore, stomatal models are often used with simple single-leaf representations of canopy radiative transfer (RT), such as big-leaf models. Nevertheless, the single-leaf canopy RT schemes do not have the capability to model optical properties of the leaves or the entire canopy. As a result, they are unable to evaluate the impact of vertical gradients within the canopy, or directly link canopy optical properties with light distribution within the canopy to remote sensing data observed from afar. Here we incorporated one optimization-based and two empirical stomatal models with a comprehensive RT model in the land component of a new Earth System model within CliMA, the Climate Modelling Alliance. The model allowed us to simultaneously simulate carbon and water fluxes as well as leaf and canopy reflectance and fluorescence spectra. We tested our model by comparing our modeled carbon and water fluxes and solar-induced chlorophyll fluorescence (SIF) to two flux tower observations (a gymnosperm forest and an angiosperm forest) and satellite SIF retrievals, respectively. All three stomatal models quantitatively predicted the carbon and water fluxes for both forests. The optimization model, in particular, showed increased skill in predicting the water flux given the lower error (c. 14.2% and 21.8% improvement for the gymnosperm and angiosperm forests, respectively) and better 1:1 comparison (slope increases from c. 0.34 to 0.91 for the gymnosperm forest, and from c. 0.38 to 0.62 for the angiosperm forest). Our model also predicted the SIF yield, quantitatively reproducing seasonal cycles for both forests. We found that using stomatal optimization with a comprehensive RT model showed high accuracy in simulating land surface processes. The ever-increasing number of regional and global datasets of terrestrial plants, such as leaf area index and chlorophyll contents, will help parameterize the land model and improve future Earth System modeling in general.



1 Introduction

Anthropogenic emissions have resulted in an unprecedentedly rapid increase in atmospheric carbon dioxide (CO₂) concentrations and thus global warming (IPCC, 2014). The land system, a big carbon sink (Quéré et al., 2018; Friedlingstein et al., 2020), slows the increase of atmospheric [CO₂] and climate change by taking up about one third of anthropogenic emissions.

25 Yet, whether the land system continues to be a carbon sink in the near future remains debatable (Anav et al., 2013; Arora et al., 2013; Jones et al., 2013; Sperry et al., 2019). Increasing tree mortality across the globe further complicates this prediction (Hartmann et al., 2015). A key to addressing this problem is to better simulate and monitor the coupled carbon, water, and energy fluxes at the land surface.

Terrestrial plants control the opening of tiny pores on leaves, called stomata, in response to a variety of environmental and physiological stimuli. Accurately representing this process is therefore essential in land surface simulations, as stomata affect carbon and water fluxes as well as the surface energy balance. In the past decades, many stomatal models, based either on statistical regressions (e.g., Ball et al., 1987; Leuning, 1995; Medlyn et al., 2011) or optimization theories (e.g., Cowan and Farquhar, 1977; Wolf et al., 2016; Sperry et al., 2017; Mencuccini et al., 2019; Wang et al., 2020), have been proposed and used to model leaf-level stomatal responses. The empirical models are computationally efficient and well-represent stomatal responses to the environmental cues in the absence of water stress, and are thus widely used in land surface models. Yet, these empirical models rely on ad-hoc tuning factors to force stomatal response to drought (Powell et al., 2013), which introduces additional uncertainty in carbon cycle modeling (Trugman et al., 2018).

In comparison, trait-based stomatal optimization models predict stomatal behavior based on the trade-off between benefits of carbon gain and risk of water loss from stomatal opening (Wolf et al., 2016; Wang et al., 2020). For instance, when the soil gets drier, the risk of transporting the same amount of water increases due to a higher risk of xylem cavitation (Sperry et al., 2017), while the carbon gain remains unchanged. As a result, plants ought to reduce stomatal opening and thus water loss to balance gain and risk. A major advantage of the stomatal optimization models is that they couple environmental stress (from both the atmosphere and soil) to plant physiology, and thus more accurately represent mechanistic processes while also being less dependent on statistically fitted parameters. In particular, stomatal optimization models based on plant hydraulics have shown great potential in predicting leaf- and tree-level stomatal behavior at multiple scales, ranging from potted saplings to common garden and natural forest stands (Anderegg et al., 2018; Venturas et al., 2018; Wang et al., 2019). Also, attempts to employ the optimization theory at the regional scale showed improved predictive skills compared to empirical stomatal models (Eller et al., 2020; Sabot et al., 2020). Furthermore, optimization theory can be readily extended to explain and model nighttime stomatal responses to the environment (Wang et al., 2021).

50 While traits used in stomatal optimization models improve predictive skill, the number of traits required for parameterization makes it impractical to apply them at large spatial scales. As a result, stomatal optimization models have not been rigorously evaluated at the stand level or larger spatial scales. Eddy covariance measurements of carbon, water vapor, energy exchange, and environmental conditions give a good estimate of stand level fluxes and provide a platform to test stomatal theories at the ecosystem level (Baldocchi et al., 2001; Baldocchi, 2020). Despite the often unknown plant traits and species composition



55 within a flux tower footprint, continuous and high-quality data make it possible to invert a suite of average stand-level traits. However, more investigation is required to determine how well the stomatal optimization models perform at the stand level, a gap this manuscript aims to address.

Ideally, the traits required to run stomatal optimization models can be inverted from flux tower observations. Yet, the sparse distribution of flux towers across the globe may be too sparse to provide a good estimate for how traits vary globally (Schimel et al., 2015), thus impeding the implementation of stomatal optimization theory at the landscape level. Though it is possible to interpolate these traits using climate as a driving force as done by Jung et al. (2020), these interpolated parameters cannot be verified in terms of carbon and water flux measurements directly. The growing amount of remote sensing data, such as canopy reflectance and fluorescence-based products, provides an alternative way to verify model parameterization (Schimel et al., 2019). For instance, solar-induced chlorophyll fluorescence (SIF) and near infrared reflectance of vegetation correlate with plant productivity (Frankenberg et al., 2011; Sun et al., 2018; Badgley et al., 2019). Furthermore, it is possible to directly compare model predicted reflectance and fluorescence spectra to satellite observations.

To date, all stomatal optimization models are used with simple canopy radiative transfer (RT) schemes due to their simplicity and efficiency (including the big leaf model which partitions the canopy into sunlit and shaded fractions; Campbell and Norman, 1998). The single leaf representation of the canopy, however, cannot be used to simulate the reflectance or fluorescence of the entire canopy, which requires bidirectional radiation within the canopy to be simulated. More complex models with more detailed representations of the canopy RT scheme are therefore required for the purpose of simulating canopy optical parameters, such as the radiative transfer scheme used in the Soil-Canopy Observation of Photosynthesis and Energy fluxes model (mSCOPE; Yang et al., 2017).

Here, we aim to advance land surface modeling by incorporating a recently developed stomatal optimization model (Wang et al., 2020) and the mSCOPE RT concept. With the advanced land model, we were able to link both plant productivity and canopy optical parameters to stomatal optimization theory. We evaluated our model by comparing the model predicted ecosystem carbon and water fluxes to flux tower measurements, and the model predicted SIF to TROPospheric Monitoring Instrument (TROPOMI) SIF retrievals (Köhler et al., 2018).

2 Model description

80 We present our first step towards bridging stomatal control, plant hydraulics, and a comprehensive RT scheme in the land component of a new Earth System model developed by the Climate Modeling Alliance (CliMA). The CliMA Land model addresses soil water movement, plant water transport, stomatal regulation, canopy radiative transfer, and water, carbon, and energy fluxes in a highly modular manner (i.e., each component can be used as a stand-alone package). Code and documentation of the in-development CliMA Land model are freely and publicly available at <https://github.com/CliMA/Land>. In the sections below, we introduce the model framework by highlighting improvements and modifications to existing vegetation model components.



2.1 Plant Architecture

Here, we treated a site as a uniform “mono-species” stand. Therefore, a suite of average plant traits were applied to the stand, and the stand level simulation was done using these bulk traits. The average plant was represented as a tree, and the modeled tree consisted of a multi-layer root system, a trunk, and a multi-layer canopy to match the soil and canopy setups (Fig. 1a). Each root layer corresponds to a horizontal soil layer, and contains a rhizosphere component and a root xylem in series (water flows through the rhizosphere and then the root xylem). All root layers are in parallel and connected to the base of the trunk. Each canopy layer corresponds to a horizontal air layer, containing a stem and leaves in series (water flows through the stem and then the leaves). All canopy layers are in parallel and connected to the top of the trunk. We assumed an uniformly distributed leaf area in the canopy both vertically and horizontally, with leaf orientation being evenly distributed in the azimuth. At each canopy layer and azimuth angle, we further adopted a leaf inclination angular distribution. By default, the leaf inclination angle is evenly distributed from 0° to 90° . The inclusion of leaf area fraction and leaf angle distribution allows us to simulate the bidirectional radiation within the canopy.

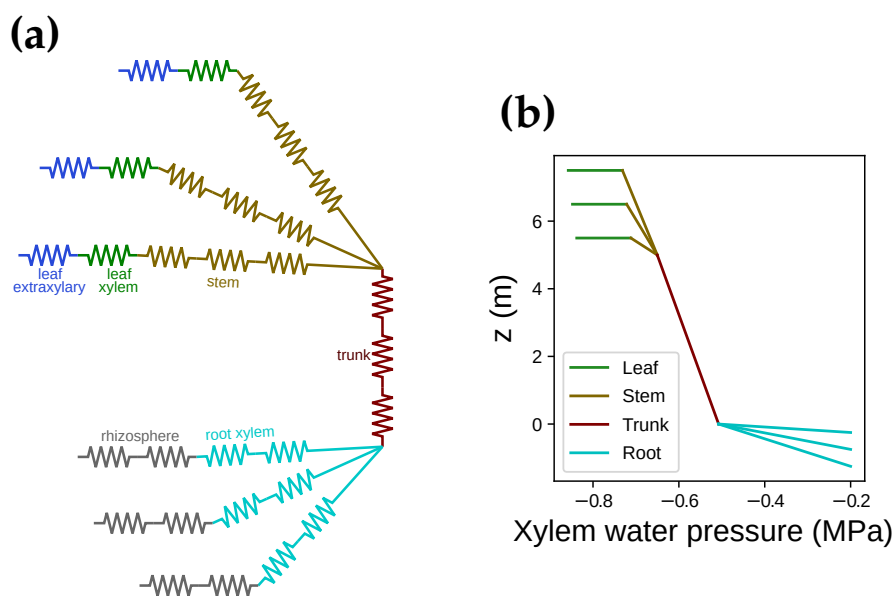


Figure 1. The hydraulic system is customized to match the canopy layers to the canopy radiation model. **(a)** An example of hydraulic system with multiple root layers, a trunk, and multiple canopy layers. **(b)** An example of xylem water pressure profile in the hydraulic system when soil water potential is -0.2 MPa for all soil layers. For better visualization, we use three root layers and three canopy layers in this example and compute the bulk mean leaf xylem pressure for all the leaves in each canopy layer. We note it here that there is an extraxylary component downstream the leaf xylem. However, as the extraxylary flow does not impact xylem hydraulic conductance, it has little impact on the stomatal models we use in our model. Yet, the extraxylary component impact leaf water potential at the evaporation site and leaf water content, and it needs to be cautious if the stomatal models are formulated using these physiology parameters.



We did not attempt to model the detailed hydraulic architecture within each root or canopy layer, and thus all transpiration within a root or canopy layer was transported via a single root or stem. All leaves in each canopy layer are in parallel and connected to the end of the stem. The hydraulic flow and pressure profile were simulated for each leaf in each canopy layer. We simulated the flow and pressure at steady state, and therefore the following criteria were met: the total transpiration rate in each canopy layer was equal to the flow rate in the stem of that layer; the total flow rate of all canopy layers was equal to the flow rate in the trunk and the total flow rate of all root layers; and the root xylem pressure at the end of each root xylem was the same (namely the pressure at the tree base; Fig. 1b).

We used constant leaf physiological parameters (such as hydraulic and photosynthetic traits) throughout the canopy, i.e., there was no difference between leaves with different azimuth or inclination angles. However, as we modeled the light environment for leaves at different layers and with different azimuth and inclination angles, we allowed the leaves to have different stomatal conductances and thus different photosynthetic rates. We note that our model framework allowed us to customize vertical leaf area distribution, leaf angular distribution, and photosynthetic capacity profile vertically. Yet, for now we used even distributions in our model simulations due to the limited knowledge of the true distributions at the study sites.

2.2 Canopy Radiative Transfer

We used the mSCOPE model RT framework (Yang et al., 2017) to simulate the light environment within the canopy. However, we made some modifications to make the model more realistic. The first difference was that we accounted for carotenoid light absorption as part of absorbed photosynthetically active radiation (APAR; Frank and Cogdell, 1996; Kodis et al., 2004; Koyama et al., 2004). When accounting for carotenoids, APAR-related absorption relative to the total pigment absorption increases in the wavelength range from 400 to 550 nm (Fig. 2a). APAR thus increases for all leaves in each canopy layer because of the carotenoid absorption (an example in Fig. 2b). This extra light absorption by carotenoid drives increases in both SIF and gross primary productivity. As a result, our modeled photosynthetic rate and fluorescence ought to be higher than the original mSCOPE model for the same model setup.

The second difference was that we accounted for the bidirectional reflectance distribution function effect of canopy horizontal structure by incorporating a clumping index (CI; Braghieri et al., 2021). As CI impacts the effective leaf area index (eLAI for effective value, and LAI for the true value) of an open canopy (Pinty et al., 2006; Braghieri et al., 2019, 2020): $eLAI = LAI \cdot CI$, we used eLAI in our model, whereas the original mSCOPE used LAI. When $CI = 1$, leaves are uniformly distributed in the horizontal; when $CI < 1$, there are gaps between and within clusters of leaves for each tree. The inclusion of a $CI < 1$ under low soil albedo values (we used a constant soil albedo of 0.2 in our model) results in a higher sunlit leaf fraction for every canopy layer, lower APAR for upper canopy layers, higher APAR for lower canopy layers, a different reflectance spectrum, and lower SIF (Fig. 3).

In the model simulations, we (1) calibrated the leaf chlorophyll fluorescence, reflectance, and transmittance spectra using the FLUSPECT-B model (Vilfan et al., 2016); (2) computed canopy optical properties (extinction coefficients for direct and diffuse light) from leaf inclination and azimuth distribution functions and sun-sensor geometry (Yang et al., 2017); (3) computed scattering coefficient matrices for direct and diffuse light based on the extinction coefficients and leaf reflectance and

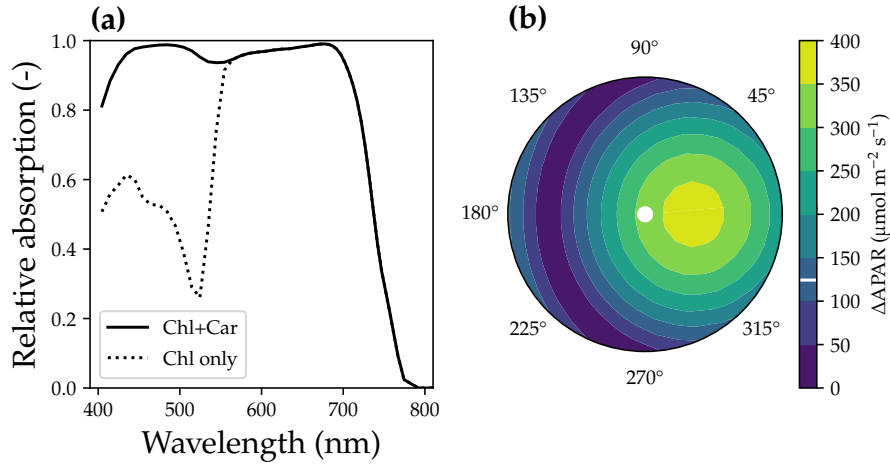


Figure 2. Impact of carotenoid light absorption on absorbed photosynthetically active radiation (APAR). **(a)** Fraction of APAR light absorption relative to all pigment absorption. The solid curve represents the scenario when both chlorophyll and carotenoid absorption are counted as APAR. Dashed curve plots the scenario when only chlorophyll absorption is counted as APAR. **(b)** APAR difference between the two scenarios for leaves with different azimuth angles (0° to 360°) and inclination angles (axial direction, from 0° to 90°). The colors indicate the increase of APAR for sunlit leaves with different angles when accounting carotenoid absorption as APAR. White line on the color bar indicates the increase of APAR for shaded leaves. The results are from the top canopy layer out of 20 layers for a canopy with leaf area index of 3, clumping index of 1, and solar zenith angle of 30° .

transmission spectra; (4) simulated the shortwave radiation through the canopy; (5) computed a variety of integrated fluxes, such as absorbed soil radiation and direct and diffuse APAR per layer (including angles for direct light); (6) calculated the steady state stomatal conductance based on different stomatal models for each leaf angle, and then the fluorescence quantum yield from leaf photosynthesis; and (7) computed the four-stream radiation transport for SIF.

In the model, we represented leaf azimuth angle from 0° to 360° at 10° increment steps ($N_{azi} = 36$), leaf inclination angle from 0° to 90° at 10° increment steps ($N_{incl} = 9$). At each time step, we were able to calculate the fraction of sunlit leaf ($f_{azi,incl}$) and APAR for each leaf angle combination (azimuth and inclination; e.g., Fig. 3). Therefore, we had a total of $N_{azi} \times N_{incl} + 1$ APAR values in each canopy layer (1 for shaded leaf fraction), and the probability of each APAR value per layer was

$$p_{azi,incl,n} = \frac{1}{N_{azi} \cdot N_{incl}} \cdot f_{azi,incl,n} \quad (1)$$

$$p_{shade,n} = 1 - \sum_{1 \leq azi \leq N_{azi}; 1 \leq incl \leq N_{incl}} (p_{azi,incl,n}) \quad (2)$$

where $p_{azi,incl,n}$ is the fraction of sunlit part for the “azi”th azimuth angle and “incl”th inclination angle at the “n”th canopy layer (N_{lay} layers in total), and $p_{shade,n}$ is the fraction of shaded part in the “n”th layer. Also, we had canopy reflectance and fluorescence spectra from a prescribed observation angle, from which we calculated SIF at 740 nm (SIF_{740}).

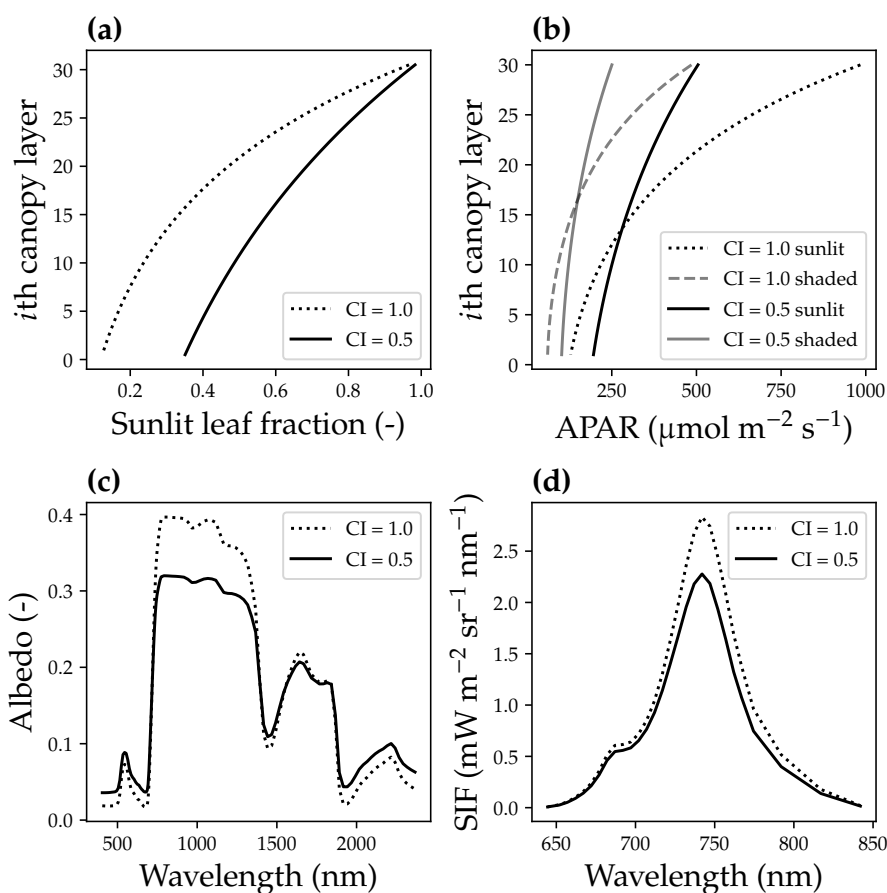


Figure 3. Impact of canopy clumping on canopy radiative transfer. (a) Impact of canopy clumping index (CI) on sunlit leaf fraction. (b) CI impacts on mean sunlit and shaded leaf absorbed photosynthetic radiation (APAR). (c) CI impacts on canopy reflectance spectrum. (d) CI impacts on solar-induced chlorophyll fluorescence spectrum. The model simulation was done using a canopy with a leaf area index of 3, 30 canopy layers, a solar zenith angle of 30° , a viewing zenith angle of 0° , and a constant fluorescence yield of 1%.



145 2.3 Stomatal Models

We used one optimization-based (Wang et al., 2020) and two empirical stomatal models (Ball et al., 1987; Medlyn et al., 2011) along with our modified version of the mSCOPE RT scheme. For the optimization-based stomatal model (OSM), we calculated the steady state stomatal conductance per leaf per canopy layer by maximizing the difference between the leaf level carbon gain (represented by the net photosynthetic rate modeled using classic Farquhar et al. (1980) model for C3 plants, A_{net} in $\mu\text{mol CO}_2 \text{ m}^{-2} \text{ s}^{-1}$) and a risk (represented via leaf hydraulics and photosynthesis):

$$\underbrace{A_{\text{net}}}_{\text{gain}} - \underbrace{A_{\text{net}} \cdot \frac{E}{E_{\text{crit}}}}_{\text{risk}} \quad (3)$$

where E is leaf level transpiration rate in $\text{mol m}^{-2} \text{ s}^{-1}$, and E_{crit} is the critical transpiration rate for that leaf in $\text{mol m}^{-2} \text{ s}^{-1}$, beyond which the leaf hydraulic conductance drops to 0.1% of the maximum value (Sperry and Love, 2015). Note that with the ascent of sap along the xylem, xylem water pressure becomes more negative (Fig. 1b), and the xylem hydraulic conductance decreases as a result of cavitation (Sperry and Tyree, 1988). The higher the leaf transpiration rate, the more negative leaf xylem pressure is at the end of the leaf xylem in order to match transpiration and resupply of water to the leaf from the root system. However, leaf transpiration rate cannot be infinitely high because of xylem cavitation at negative xylem pressures. For example, for a leaf with a given xylem pressure at the leaf base (Ψ_{base}), E peaks while leaf xylem pressure gets more and more negative (Fig. 4a), and E higher than this peak is physically unreachable.

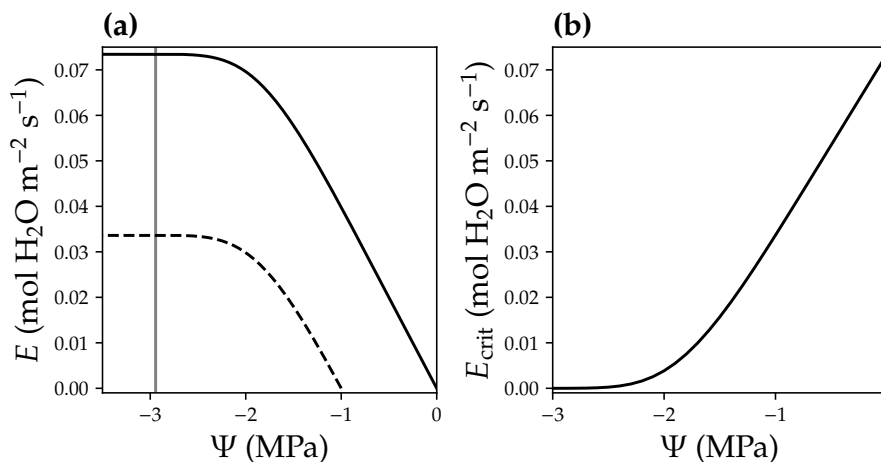


Figure 4. Leaf critical flow rate changes with leaf base xylem pressure. (a) Leaf xylem water supply curves at two different leaf base xylem pressures (Ψ_{base} ; black solid curve for a $\Psi_{\text{base}} = 0$ MPa and black dashed curve for a $\Psi_{\text{base}} = -1$ MPa). A xylem water supply curve is the plot of leaf xylem flow rate (E) vs. leaf xylem end pressure (Ψ) at a given Ψ_{base} ($\Psi = \Psi_{\text{base}}$ when $E = 0$). The gray vertical line plots the xylem pressure at which leaf xylem conductance reaches 0.1% of the maximum. The intersection of the gray line and xylem water supply curve indicates the critical xylem flow rate (E_{crit}). (b) E_{crit} decreases with more negative Ψ_{base} .



160 We defined the transpiration rate at which leaf xylem hydraulic conductance decreases to 0.1% of the maximum value as E_{crit}
 in our model (namely at 99.9% loss of hydraulic conductance; Fig. 4a). We used a hybrid Bisection-Newton method algorithm
 provided by `ConstrainedRootSolvers.jl` (<https://github.com/Yujie-W/ConstrainedRootSolvers.jl>) to numerically compute E_{crit}
 (through solving the intersection of the gray line and xylem water supply curve in Fig. 4a). E_{crit} decreases when Ψ_{base} becomes
 more negative (Fig. 4; e.g., as a result of drier soil). The use of E_{crit} in the risk function (equation 3) allowed us to predict
 165 stomatal response to soil drought, because lower E_{crit} resulted higher risk. See Fig. 5 for the theoretical whole plant responses
 to the environmental stimuli for OSM. Note that though equation 3 is the same as that in Wang et al. (2020), the two differ in
 that equation 3 uses leaf-level flow rates so as to use with our adapted mSCOPE RT model, whereas Wang et al. (2020) model
 uses whole plant-level flow rates to use with the big leaf model.

For the Ball et al. (1987) stomatal model (BBM), we calculated the steady state stomatal conductance (g_{sw} in $\text{mol m}^{-2} \text{s}^{-1}$)
 170 using an empirical formulation:

$$g_{sw} = g_0 + g_1 \cdot \text{RH} \cdot \frac{A_{net}}{C_s} \quad (4)$$

where RH is the relative humidity of the air (fraction; unitless), C_s is the leaf surface CO_2 concentration in $\mu\text{mol mol}^{-1}$ (after
 accounting for leaf boundary layer conductance as a function of wind speed), and g_0 (in $\text{mol m}^{-2} \text{s}^{-1}$) and g_1 (unitless) are
 fitting parameters for BBM. For Medlyn et al. (2011) model (MED), the formulation reads

$$175 \quad g_{sw} = g_0 + 1.6 \cdot \left(1 + \frac{g_1}{\sqrt{D}}\right) \cdot \frac{A_{net}}{C_a} \quad (5)$$

where D is the leaf-to-air vapor pressure deficit in kPa, and C_a is the atmospheric CO_2 concentration in $\mu\text{mol mol}^{-1}$, and g_0
 (in $\text{mol m}^{-2} \text{s}^{-1}$) and g_1 (in $\sqrt{\text{kPa}}$) are fitting parameters for MED. Note that these empirical stomatal models (BBM and
 MED) do not respond to soil moisture. To account for the soil moisture response, we followed the Community Land Model
 Version 5 (CLM5) approach by attenuating photosynthetic capacity via a stress factor (β_w ; Kennedy et al., 2019):

$$180 \quad \beta_w = \frac{K}{K_{max}} \quad (6)$$

where K is the leaf hydraulic conductance calculated using the leaf xylem pressure, and K_{max} is the maximal leaf hydraulic
 conductance. The use of a tuning factor helps address the stomatal response to soil moisture for BBM and MED. Note here
 that the tuning factor is applied per leaf per canopy layer. See Fig. 5 for the theoretical whole plant responses to environmental
 stimuli for BBM and MED.

185 For each of the three stomatal models (BBM, MED, and OSM), with the steady state stomatal conductance for each APAR
 value, we computed the corresponding leaf net photosynthetic rate using the classic C3 photosynthesis model (Farquhar et al.,
 1980). The whole canopy net primary productivity (CNPP, at an instant time) was then computed using

$$\text{CNPP} = \frac{\text{LAI}}{N_{lay}} \cdot \left\{ \sum_{azi, incl, n} [A_{net} \cdot p_{azi, incl, n}] + \sum_n [A_{net} \cdot p_{shade, n}] \right\} \quad (7)$$

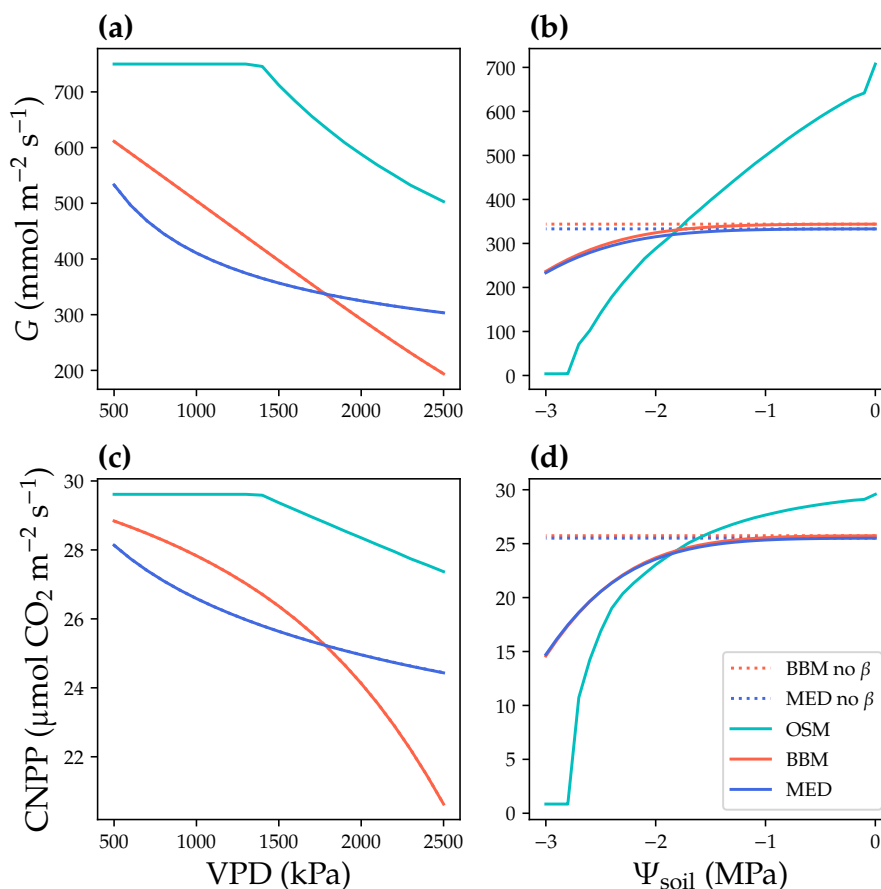


Figure 5. Responses to environmental cues of three stomatal models. The stomatal models are Ball et al. (1987), Medlyn et al. (2011), and Wang et al. (2020) stomatal model predictions (BBM, MED, and OSM), respectively. (a) Canopy cumulative stomatal conductance per ground area (G) response to atmospheric vapor pressure deficit (VPD). Red and blue dotted lines plot the responses of BBM and MED models without a tuning factor (β) for photosynthetic capacity, respectively. Red and blue solid lines plot the response of BBM and MED models with a tuning factor for photosynthetic capacity (equation 6), respectively. Cyan solid line plots the response of OSM model. The turning point around VPD = 1400 Pa is because leaf stomatal conductance hits the maximum structural limitation ($0.2 \text{ mol m}^{-2} \text{ s}^{-1}$ in the example). (b) G responses soil water potential (Ψ_{soil}). (c–d) Canopy net primary productivity per ground area (CNPP, total canopy net photosynthetic rate per ground area, gross primary productivity minus canopy leaf respiration) responses to VPD and Ψ_{soil} .



3 Carbon and water fluxes

190 3.1 Flux tower sites

We used data from two flux tower sites to test the CLiMA Land model. The first study site is located at a subalpine forest of the Niwot Ridge AmeriFlux core site (US-NR1) in the Rocky mountains in Colorado, USA (40.03°N, 105.55°W, 3050 m above the sea level; Fig. 6). The US-NR1 flux tower is surrounded by three dominate evergreen gymnosperm species: *Abies lasiocarpa*, *Picea engelmannii*, and *Pinus contorta* (Monson et al., 2002). The second study site is located at a broad leaf forest of the Missouri Ozark AmeriFlux site (US-MOz, MOFLUX) in Missouri, USA (38.74°N, 92.20°W, 219 m above the sea level; Fig. 6). The US-MOz flux tower site is dominated by a deciduous angiosperm white oak (*Quercus alba*) mixed with several other deciduous species, including sugar maple (*Acer saccharum*) and hickory (*Carya spp.*) (Yang et al., 2007; Wood et al., 2019). See Table 1 and 2 for details of the US-NR1 and US-MOz sites and the values used as model inputs. Hereafter, we refer the two sites as the gymnosperm site (US-NR1) and the angiosperm site (US-MOz).

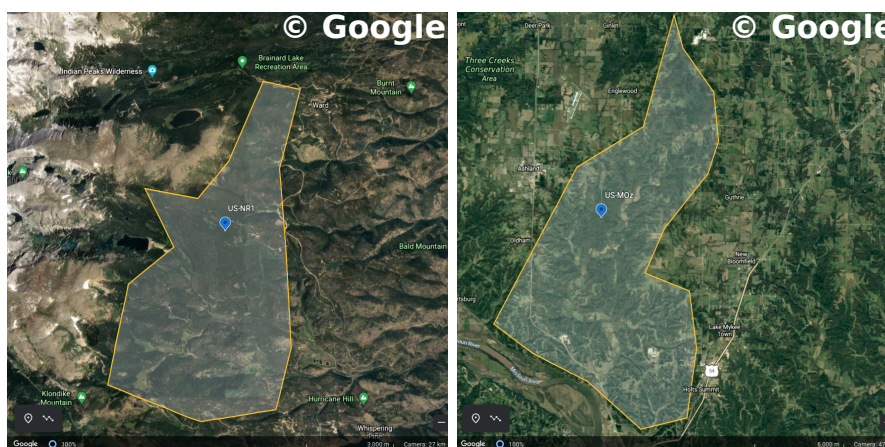


Figure 6. Regions chosen to filter TROPOMI SIF observations. Left: Google Earth map for US-NR1 flux tower site (Niwot Ridge, Colorado, USA). Right: Google Earth map for US-MOz flux tower site (Ozark, Missouri, USA). The blue symbols show the flux tower locations, and the shaded regions are representative area around the flux tower site. Maps Data: Google Landset / Copernicus.

200 3.2 Model simulations

The flux tower sites have half-hourly mean flux estimates, as well as environmental conditions since 1998 (US-NR1) and 2004 (US-MOz). We chose the data from 2006 to 2019 to test our model given the higher data quality (we omitted the year 2020 because the data was not yet available). We tested our model on an annual basis by splitting the original dataset into subsets (14 subsets for US-NR1, and 12 subsets for US-MOz given missing data on years 2006 and 2011). For each year, at each half-hour
205 time step, we simulated the steady state stomatal conductance and fluxes for the three stomatal models. To reduce uncertainty,



Table 1. Site and plant information of Niwot Ridge flux tower site.

Variable	Description	Reference
Site name	Niwot Ridge, AmeriFlux core site US-NR1	
Latitude	40.03°N	Monson et al. (2002)
Longitude	105.55°W	Monson et al. (2002)
Elevation	Height above sea level, 3050 m	Monson et al. (2002)
Canopy height	Canopy height, 12–13 m. A mean canopy height of 12.5 m was used in the model. As to the tree geometry, we assumed the trunk has a height of 6 m, and the canopy spanned from 6 to 12.5 m. We divided the canopy to 13 layers (0.5 m in height per layer).	Bowling et al. (2018)
LAI	Leaf area index, 3.8–4.2. A mean LAI of 4.0 was used in the model.	Monson et al. (2002)
Chlorophyll	Leaf chlorophyll content, 524 $\mu\text{mol m}^{-2}$	Zarter et al. (2006)
Tree density	Trees per ground area, 4000 ha^{-1} . <i>Abies lasiocarpa</i> : 16 trees per 100 m^2 ; <i>Picea engelmannii</i> : 10 trees per 100 m^2 ; <i>Pinus contorta</i> : 9 trees per 100 m^2 . Addressed by basal area per ground area (namely basal area index).	Bowling et al. (2018)
Weibull B/C	<i>A. lasiocarpa</i> : $B = 4.28 \text{ MPa}$, $C = 1.47$; <i>P. engelmannii</i> : $B = 4 \text{ MPa}$, $C = 12$; <i>P. contorta</i> : $B = 4 \text{ MPa}$, $C = 4$. Mean $B = 4.09 \text{ MPa}$ and $C = 5.82$ were used.	Tai et al. (2019)
Basal area	Mean basal area per tree. <i>A. lasiocarpa</i> : 0.063 m^2 ; <i>P. engelmannii</i> : 0.08 m^2 ; <i>P. contorta</i> : 0.144 m^2 . Total basal area per ground area for the three species are 0.031 $\text{m}^2 \text{ m}^{-2}$; and thus a mean ground area per basal area of 32.09 $\text{m}^2 \text{ m}^{-2}$ was used in the model.	Sproull (2014)
Clumping index	MODIS clumping index, 0.48. A constant CI was used in the test site because of the lack of knowledge on how CI varies with solar zenith angle in the test site.	He et al. (2012)
Root depth	Root depth, 0.4–1.0 m. A maximal root depth of 1 m was used. Yet, as we prescribed soil water content, the root depth was only used to calculate gravitational pressure drop in the roots.	Monson et al. (2002)
Soil type	Soil texture class, Cambisol. See Mello et al. (2005) for the detailed van Genuchten parameter for Cambisol type soil.	https://soilgrids.org/
Stomatal model	Ball et al. (1987) model: $g_1 = 9$; Medlyn et al. (2011) model: $g_1 = 2.35 \sqrt{\text{kPa}}$.	CLM tech notes



Table 2. Site and plant information of Missouri Ozark flux tower site (MOFLUX).

Variable	Description	Reference
Site name	Missouri Ozark AmeriFlux site, US-MOz	
Latitude	38.74°N	Yang et al. (2007)
Longitude	92.20°W	Yang et al. (2007)
Elevation	Height above sea level, 219.4 m	Yang et al. (2007)
Canopy height	Canopy height, 17–20 m. A mean canopy height of 18.5 m was used in the model. As to the tree geometry, we assumed the trunk has a height of 9 m, and the canopy spanned from 9 to 18.5 m. We divided the canopy to 19 layers (0.5 m in height per layer).	Yang et al. (2007)
LAI	Leaf area index, 4.2	Yang et al. (2007)
Chlorophyll	Leaf chlorophyll content, 57.23 $\mu\text{g cm}^{-2}$. Value is estimated from the leaf mass per area of <i>Quercus alba</i> at ambient CO ₂ (Norby et al., 2000) and chlorophyll content per mass of sunlit leaves of <i>Quercus alba</i> (Rebbeck et al., 2012).	Norby et al. (2000) Rebbeck et al. (2012)
Tree density	Trees per ground area, 583 ha ⁻¹ . Dominated by a deciduous angiosperm white oak (<i>Quercus alba</i>) mixed with several other deciduous species, including sugar maple (<i>Acer saccharum</i>) and hickory (<i>Carya spp.</i>)	Wood et al. (2019)
Weibull B/C	B = 5.703 MPa, C = 0.953.	Kannenberg et al. (2019)
Basal area	Basal area per ground area, 0.00242 m ² m ⁻² .	Yang et al. (2007)
Clumping index	MODIS clumping index, 0.69. A constant CI was used in the test site because of the lack of knowledge on how CI varies with solar zenith angle in the test site.	He et al. (2012)
Root depth	Root depth. A maximal root depth of 1 m was used. Yet, as we prescribed soil water content, the root depth was only used to calculate gravitational pressure drop in the roots.	-
Soil type	Soil texture class, Weller silt loam. van Genuchten parameters for this site was fitted using the soil moisture retention curve, where soil moisture was from flux tower measurements, and soil water potential was estimated using predawn leaf water potential (data from https://tes-sfa.ornl.gov/node/80 ; Gu et al., 2015).	Yang et al. (2007)
Stomatal model	Ball et al. (1987) model: $g_1 = 9$; Medlyn et al. (2011) model: $g_1 = 4.45 \sqrt{\text{kPa}}$	CLM tech notes



we prescribed soil moisture, leaf temperature, and reported constant leaf area index (more details of the values we used can be found in Tables 1 and 2), and then we ran offline simulations. We inverted leaf temperature using

$$210 \quad LW_{\text{out}} = \epsilon \sigma T_{\text{leaf}}^4 \quad (8)$$

where LW_{out} is the surface emitted longwave radiation from the flux tower measurement, ϵ is the emissivity of the leaf (0.97 following Campbell and Norman, 1998), σ is the Stefan-Boltzmann constant ($5.67 \times 10^{-8} \text{ W K}^{-4}$), and T_{leaf} is the mean leaf temperature in K.

To maximally reduce the uncertainty when comparing model simulations to observations, we compared the modeled carbon
215 and water fluxes directly to flux tower estimations. Thus, we did not perform the typical step that partitions observed net ecosystem exchange of CO_2 (NEE) into gross primary productivity and ecosystem respiration. Instead, we performed the partition the ecosystem to canopy and non-canopy parts. We simulated NEE as the difference between canopy net exchange (namely CNPP) and remaining respiration (wood and soil, represented by R_{remain}): $\text{NEE} = \text{CNPP} - R_{\text{remain}}$. In this way, the daytime canopy net photosynthetic rate and nighttime respiration rate were used as CNPP, whereas the remaining respiration
220 of wood and soil was computed as a function of soil temperature (T_{soil}):

$$R_{\text{remain}} = R_{\text{base}} \cdot f(T_{\text{soil}}) = R_{\text{base}} \cdot \left(\frac{T_{\text{soil}} - 298.15}{10} \right)^{Q_{10}} \quad (9)$$

where R_{base} is the respiration normalized to a reference temperature (298.15 K in our model), $f(T_{\text{soil}})$ is the temperature correction, and Q_{10} is the exponent used for temperature correction (1.4 for angiosperm and 1.7 for a gymnosperm plant following Lavigne and Ryan, 1997).

225 At each time step, we (1) calculated soil water potential and leaf temperature from the flux tower measurements; (2) computed the solar zenith angle based on the site latitude and local time; (3) simulated the canopy radiative transfer, and obtained APAR values for sunlit and shaded leaves in each canopy layer; (4) updated environmental conditions and leaf temperature per canopy layer; (5) computed the steady state stomatal conductance for each leaf angle in each canopy layer using the classic C_3 photosynthesis model (Farquhar et al., 1980), and summed the canopy carbon and water fluxes of the entire canopy; (6) with
230 the computed steady state photosynthetic rate, we modeled leaf level fluorescence yield using van der Tol et al. (2014) model parameters and site-level SIF_{740} using the updated version of the mSCOPE model; (7) calculated R_{remain} from soil temperature using equation 9; and (8) compared site level modeled NEE and water fluxes (ET) to flux tower estimates. For the hydraulic system, we assumed the xylem hydraulic conductance recovers when soil rehydrated (in other words, we did not modeled the drought legacy effect within or across growing seasons).

235 3.3 Fit unknown parameters

Note that there were some missing essential parameters in our model: site level bulk photosynthetic capacity (represented by maximal carboxylation rate and maximal electron transport rate at a reference temperature, $V_{\text{cmax}25}$, and $J_{\text{max}25}$ at 25°C , respectively), hydraulic conductance per basal area (namely K_{max}), and R_{base} . These parameters have a large impact on model simulations as $V_{\text{cmax}25}$, $J_{\text{max}25}$, and K_{max} affect stomatal opening (and thus canopy carbon and water fluxes), and R_{base} affects



240 stand carbon flux. We note that there were some $V_{\text{cmax}25}$ and $J_{\text{max}25}$ observations for US-MOz for a few years (Gu et al., 2015), but a complete time series of the $V_{\text{cmax}25}$ and $J_{\text{max}25}$ was not available. Therefore, we fitted these parameters by minimizing the mean absolute standardized error of both carbon and water fluxes for each year:

$$\text{minimize} \quad \frac{\text{mean}(|\text{NEE}_{\text{mod}} - \text{NEE}_{\text{obs}}|)}{\text{std}(|\text{NEE}_{\text{obs}}|)} + \frac{\text{mean}(|\text{ET}_{\text{mod}} - \text{ET}_{\text{obs}}|)}{\text{std}(\text{ET}_{\text{obs}})} \quad (10)$$

where subscripts “mod” and “obs” represent model and observation, respectively. Note that we fitted $V_{\text{cmax}25}$ ($J_{\text{max}25} = 1.67 \cdot V_{\text{cmax}25}$), K_{max} (we assumed a constant root:stem:leaf resistance ratio of 2:1:1), and R_{base} for each stomatal model to make fair comparison of three models. We used only the flux data from growing season of each year, and the growing season period was defined as the time when the mean daily carbon flux was higher than $1 \mu\text{mol m}^{-2} \text{s}^{-1}$ for seven consecutive days. Note that a constant $V_{\text{cmax}25}$ was used for all three models rather than a time series. However, because of the model setup, OSM used constant $V_{\text{cmax}25}$ throughout the growing season, whereas BBM and MED used variable effective $V_{\text{cmax}25}$ as a result of the tuning factor to account for stomatal response to soil moisture. See Figs. 7 and 8 for the examples of the fitted results for the gymnosperm and angiosperm forests, respectively.

3.4 Model performance

All three stomatal models (one optimization-based and two empirical) were able to track the diurnal and seasonal carbon and water fluxes (e.g., Fig. 7 for gymnosperm site and Fig. 8 for angiosperm site). In general, all three models quantitatively predicted the net ecosystem carbon flux (Figs. 7a,c, 8a,c, 9, 10). However, predicted water fluxes diverged across the models, as the BBM and MED models tended to underestimate water fluxes, and the OSM model better matched the magnitude of water flux (Figs. 7b,d, 8b,d). See Figures S1–S26 for the comparison of time series of carbon and water fluxes for each site at each growing season.

3.4.1 Fitting parameter variation

260 The same amount of variables: $V_{\text{cmax}25}$, R_{base} , and K_{max} were fitted for all three stomatal models. In terms of fitting parameter variation, in general, OSM had the lowest standard deviation, whereas BBM and MED had higher standard deviation (Figs. 9a, 10a; Table 3). In terms of MASE, OSM had the lowest error (sum for both carbon and water fluxes), whereas BBM and MED had higher error (Figs. 9b, 10b; Table 4).

While all three stomatal models had similar fitted soil respiration (R_{base}), the models had divergent fitted photosynthetic capacity ($V_{\text{cmax}25}$) and maximal hydraulic conductance (K_{max}). In general, the empirical models required higher $V_{\text{cmax}25}$ (Figs. 9a and 10a). The reason is that the empirical models in the present study were used along with a tuning factor for effective $V_{\text{cmax}25}$ (Kennedy et al., 2019). In comparison, the stomatal optimization model weighs the carbon gain and risk trade-off to determine stomatal opening, and effective $V_{\text{cmax}25}$ is held constant throughout the simulation. Thus, for empirical models, leaf-level effective $V_{\text{cmax}25}$ is always lower than the fitted value because of the negative leaf xylem pressure.

270 We note that varying effective $V_{\text{cmax}25}$ based on leaf hydraulic conductance loss is only one form of the ad-hoc tuning factor to force stomatal responses to drought (e.g., see Powell et al. (2013), Trugman et al. (2018), and Kennedy et al. (2019) for

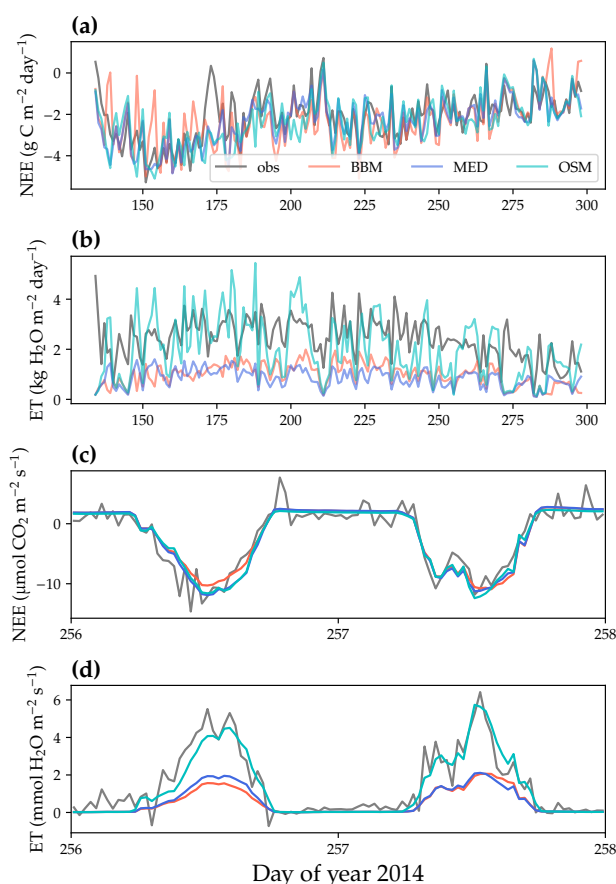


Figure 7. Comparison of model predicted carbon/water fluxes to US-NR1 (Niwot Ridge, evergreen gymnosperm forest) flux tower observations for year 2014. **(a)** Gray curve plots the daily CO_2 flux in the growing season. Shaded red, blue, and cyan curve each plots the Ball et al. (1987), Medlyn et al. (2011), and Wang et al. (2020) stomatal model predictions (BBM, MED, and OSM), respectively. **(b)** Comparison of modeled and observed daily total transpiration flux. **(c)** Comparison of half-hourly modeled and observed net ecosystem carbon flux (NEE) for days 256–257 of year 2014. **(d)** Comparison of modeled and observed ecosystem water flux (ET) for days 256–257 of year 2014.

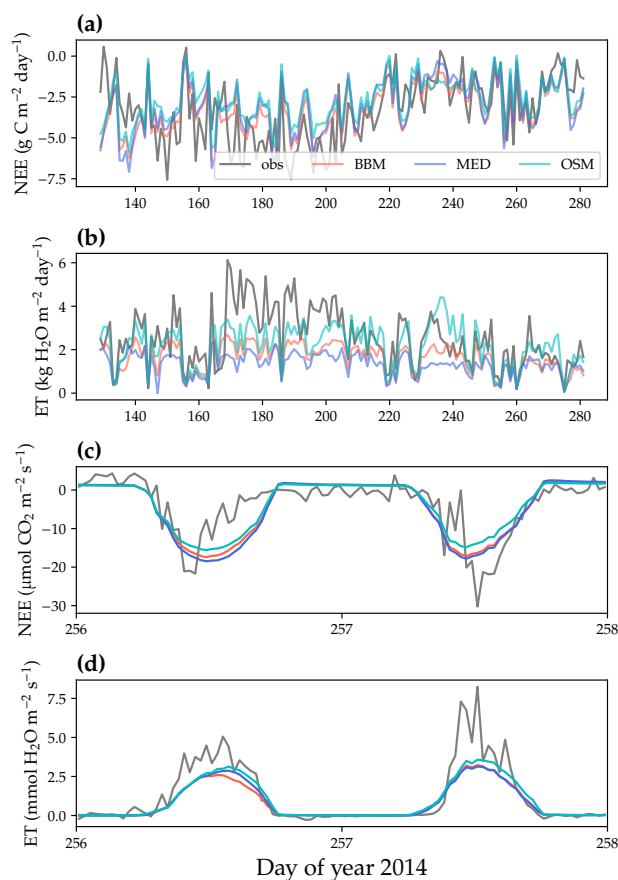


Figure 8. Comparison of model predicted carbon/water fluxes to US-MOz (MOFLUX, deciduous angiosperm forest) flux tower observations for year 2014. **(a)** Gray curve plots the daily CO_2 flux in the growing season. Shaded red, blue, and cyan curve each plots the Ball et al. (1987), Medlyn et al. (2011), and Wang et al. (2020) stomatal model predictions (BBM, MED, and OSM), respectively. **(b)** Comparison of modeled and observed daily total transpiration flux. **(c)** Comparison of half-hourly modeled and observed net ecosystem carbon flux (NEE) for days 256–257 of year 2014. **(d)** Comparison of modeled and observed ecosystem water flux (ET) for days 256–257 of year 2014.

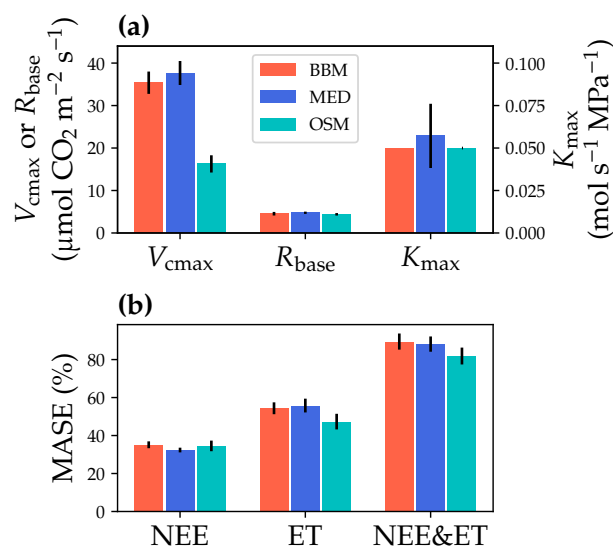


Figure 9. Comparisons of fitted model parameters and model predictive skills for US-NR1 (Niwot Ridge, evergreen gymnosperm forest) flux tower. **(a)** Red bars plot the mean of fitted parameters for Ball et al. (1987) stomatal model (BBM). The fitting parameters are maximal carboxylation rate 25 °C (V_{cmax25}), soil respiration rate at 25 °C (R_{base}), and maximal whole plant hydraulic conductance (K_{max}). Blue and cyan bars plot the means for Medlyn et al. (2011) (MED) and Wang et al. (2020) (OSM) models, respectively. Black error bars plot the standard deviation of the fitting parameter. **(b)** Comparison of mean absolute standardized error (MASE, equation 10) for carbon flux (NEE), water flux (ET), and both NEE and ET.

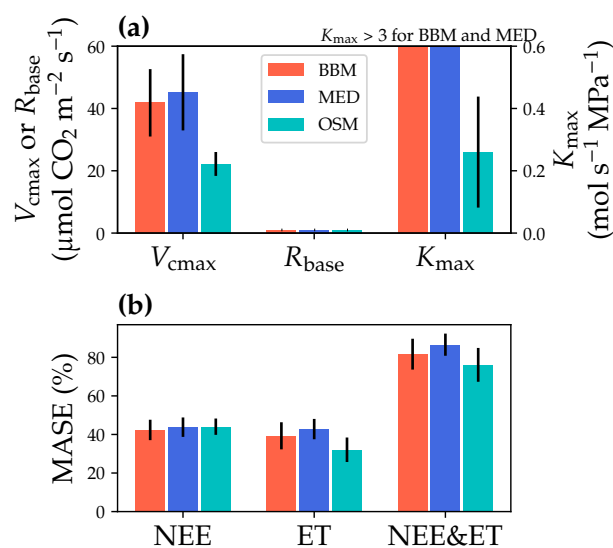


Figure 10. Comparisons of fitted model parameters and model predictive skills for US-MOz (MOFLUX, deciduous angiosperm forest) flux tower. **(a)** Red bars plot the mean of fitted parameters for Ball et al. (1987) stomatal model (BBM). The fitting parameters are maximal carboxylation rate 25 °C (V_{cmax25}), soil respiration rate at 25 °C (R_{base}), and maximal whole plant hydraulic conductance (K_{max}). Blue and cyan bars plot the means for Medlyn et al. (2011) (MED) and Wang et al. (2020) (OSM) models, respectively. Black error bars plot the standard deviation of the fitting parameter. The fitted K_{max} of BBM and MED reaches the maximum limit of K_{max} ranges ($4 \text{ mol H}_2\text{O s}^{-1} \text{ MPa}^{-1}$), and is way higher than that of OSM; thus the bars are cut off to compare with the OSM. **(b)** Comparison of mean absolute standardized error (MASE, equation 10) for carbon flux (NEE), water flux (ET), and both NEE and ET.



Table 3. Fitting parameters of three stomatal models. the models are Ball et al. (1987) model (BBM), Medlyn et al. (2011) model (MED), and Wang et al. (2020) model (OSM). Numbers show in the table are mean \pm standard deviation. The fitted parameters include: maximum carboxylation rate at 25 °C ($V_{\text{cmax}25}$), root respiration at 25 °C (R_{base}), maximal tree hydraulic conductance per basal area (K_{max}), and empirical stomatal parameter g_1 (unitless for BBM, in $\sqrt{\text{kPa}}$ for MED).

Site	Model	$V_{\text{cmax}25}$	R_{base}	K_{max}	g_1
		$\mu\text{mol m}^{-2} \text{s}^{-1}$		$\text{mol m}^{-2} \text{s}^{-1} \text{MPa}^{-1}$	- or $\sqrt{\text{kPa}}$
When g_1 was not fitted for BBM and MED					
Niwot Ridge	BBM	35.4 \pm 2.6	4.5 \pm 0.4	0.050 \pm 0.000	-
	MED	37.7 \pm 2.8	4.8 \pm 0.3	0.057 \pm 0.019	-
	OSM	16.3 \pm 2.0	4.4 \pm 0.3	0.050 \pm 0.000	-
MOFLUX	BBM	41.8 \pm 10.8	1.0 \pm 0.0	4.000 \pm 0.000	-
	MED	45.2 \pm 12.2	1.0 \pm 0.0	4.000 \pm 0.000	-
	OSM	22.2 \pm 3.8	1.0 \pm 0.0	0.260 \pm 0.178	-
When g_1 was fitted for BBM and MED					
Niwot Ridge	BBM	21.8 \pm 1.5	5.1 \pm 0.5	0.093 \pm 0.018	18.5 \pm 1.4
	MED	21.1 \pm 1.2	4.8 \pm 0.3	0.054 \pm 0.013	6.5 \pm 0.5
	OSM	16.3 \pm 2.0	4.4 \pm 0.3	0.050 \pm 0.000	-
MOFLUX	BBM	30.4 \pm 7.8	1.1 \pm 0.2	4.000 \pm 0.000	23.9 \pm 14.5
	MED	30.8 \pm 7.9	1.1 \pm 0.2	4.000 \pm 0.000	16.0 \pm 9.3
	OSM	22.2 \pm 3.8	1.0 \pm 0.0	0.260 \pm 0.178	-



Table 4. Statistics of three stomatal model predictive skills. The models are Ball et al. (1987) model (BBM), Medlyn et al. (2011) model (MED), and Wang et al. (2020) model (OSM). The NEE section shows the regression details of modeled versus observed net ecosystem carbon flux (NEE); whereas the ET section shows the regression details of modeled versus observed ecosystem water flux (ET). Row “MASE” shows the mean absolute standardized error (mean for each year). Row “ $P_{\text{slope}=1}$ ” indicates the P value for whether the slope is different from 1. Columns “BBM-g” and “MED-g” display the results when an extra empirical parameter “ g_1 ” (equations 4 and 5) is also fitted for the empirical model.

Model	Niwot Ridge					MOFLUX				
	BBM	MED	OSM	BBM-g	MED-g	BBM	MED	OSM	BBM-g	MED-g
NEE										
MASE	35.1%	32.4%	34.5%	33.6%	33.4%	42.3%	43.8%	44.0%	42.2%	42.2%
R^2	0.78	0.82	0.78	0.79	0.79	0.62	0.60	0.60	0.62	0.62
Intercept	0.32	0.37	0.47	0.32	0.37	1.16	1.04	1.12	1.41	1.44
Slope	0.88	0.90	0.84	0.83	0.79	0.63	0.63	0.52	0.59	0.60
$P_{\text{slope}=1}$	All < 0.001									
ET										
MASE	54.4%	55.8%	47.3%	38.7%	37.9%	39.3%	42.8%	32.1%	28.7%	29.3%
R^2	0.58	0.66	0.58	0.64	0.66	0.74	0.72	0.73	0.75	0.73
Intercept	8.0E-5	8.2E-5	9.6E-5	1.4E-4	1.4E-4	2.5E-4	2.5E-4	3.9E-4	3.7E-4	3.9E-4
Slope	0.35	0.32	0.91	0.69	0.65	0.41	0.34	0.62	0.69	0.62
$P_{\text{slope}=1}$	All < 0.001									



alternative formulations). The advantage of a $V_{\text{cmax}25}$ tuning factor is that it helps account for the decreasing effective $V_{\text{cmax}25}$ during drought (either due to real drop in photosynthetic capacity or mesophyll conductance; Dewar et al., 2018), and thus could be more realistic in water limiting scenarios; however, tuning effective $V_{\text{cmax}25}$ for short term changes in leaf water potential may harm the model performance (such as diurnal changes of leaf water potential when there is no soil drought; Wang et al., 2020). In comparison, the OSM used a constant $V_{\text{cmax}25}$ throughout a growing season, and would not be able to capture the decrease of $V_{\text{cmax}25}$ if it happens. Despite the fact that $V_{\text{cmax}25}$ does decrease during drought (e.g., Zhou et al., 2014, 2016), there is no direct evidence that $V_{\text{cmax}25}$ varies linearly with leaf water potential, plant/leaf hydraulic conductance, soil moisture, or soil water potential for all species. Better understanding of how $V_{\text{cmax}25}$ varies during and after a drought will improve the accuracy in modeling carbon and water fluxes for all stomatal models.

The fitted K_{max} was comparable for all three models at the gymnosperm site, but was much higher for empirical models at the angiosperm site. The reason for this contrasting behavior was also the tuning factor based on hydraulic conductivity loss. The xylem vulnerability curve in our model was represented by a Weibull function: $k_x = k_{x,\text{max}} \cdot \exp[-(-P/B)^C]$, where B indicates the xylem pressure at c. 63% loss of conductivity and C indicates the steepness of the decrease in k . Though the tested angiosperm forest had a higher $B = 5.70$ MPa compared to 4.09 MPa of the gymnosperm forest, $C = 0.95$ of angiosperm site was much lower than that of gymnosperm site (5.82). As a result, effective $V_{\text{cmax}25}$ used in BBM and MED models dropped dramatically at relatively less negative soil water potential for the angiosperm site (e.g., > -2 MPa), while the effective $V_{\text{cmax}25}$ barely changed for the gymnosperm site. At the default g_1 setting, the empirical models underestimate water flux, and thus the optimized K_{max} would be higher to increase the canopy water flux. Yet, we note that the error does not change much for very high K_{max} because the water flux is mainly controlled by the g_1 parameter in the empirical models.

3.4.2 Quantitative comparison

In terms of minimal under- or overestimation, OSM showed the highest predictive skill because of the better performance in predicting water fluxes. For the gymnosperm site, combining all data and simulation from 14 growing seasons from 2006 to 2019, we found that model predicted carbon fluxes were overall near 1:1 compared to flux tower observations for all the three models (Fig. 11a–c). However, the slopes of the linear regressions (red lines in Fig. 11a–c) for carbon flux were all significantly lower than 1 (despite that the slopes were close to 1; $P < 0.001$; more detailed statistics in Table 4). As for the water flux, all three models underestimated water fluxes compared to the flux tower observations (Fig. 11d,e), and the slopes were all significantly lower than 1 ($P < 0.001$; Table 4). The stomatal optimization model based on plant hydraulics (OSM), however, better predicted the water flux (Fig. 11f) compared to the empirical models. We found similar pattern for the angiosperm site (Fig. 12; Table 4). The model performances were in general slightly worse in MOFLUX, given the higher error in predicted NEE and shallower slope for both NEE and ET. The relatively worse performances were likely due to the higher variation in observed NEE and ET, e.g., many NEE observations were higher than $10 \mu\text{mol m}^{-2} \text{s}^{-1}$.

Our model simulations suggest that implementing plant hydraulic trait-based stomatal optimization model into vegetation models has great potential in improving the model predictive skills, particularly for the water flux (Figs. 11 and 12), adding new evidences to existing literature (e.g., Anderegg et al., 2018; Venturas et al., 2018; Wang et al., 2019; Eller et al., 2020;

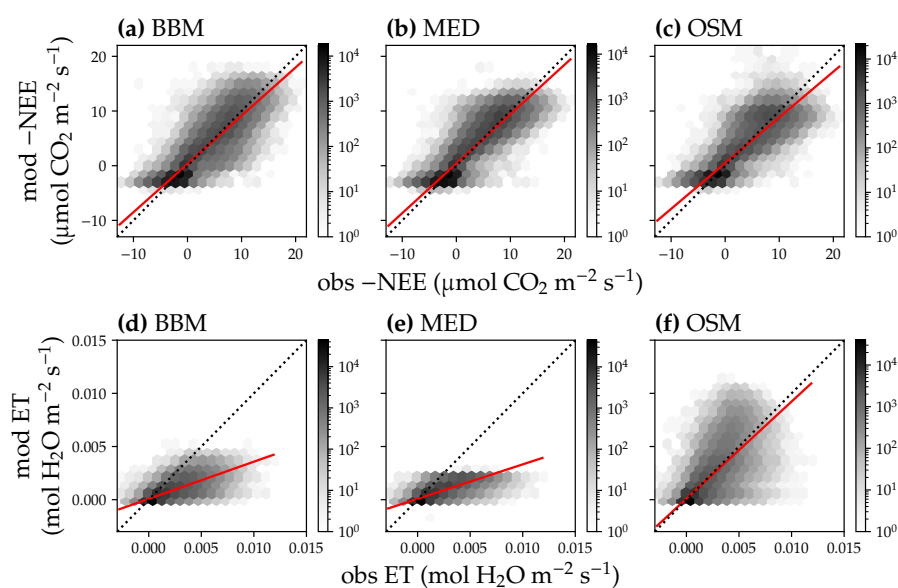


Figure 11. Comparison of half-hourly modeled and observed carbon and water fluxes for three stomatal models for US-NR1 (Niwoot Ridge, evergreen gymnosperm forest) flux tower. (a) Comparison of modeled (y axis) and observed (x axis) net ecosystem carbon flux (NEE) for Ball et al. (1987) stomatal model (BBM). Shading represents density; the darker the hexagon, the more data that fell within the hexagon. The red solid line plots the linear regression of the data, and the black dotted line plots the 1:1 line. (b) Comparison of NEE for Medlyn et al. (2011) model (MED). (c) Comparison of NEE for Wang et al. (2020) model (OSM). (d) Comparison of ecosystem water flux (ET) for BBM. (e) Comparison of ET for MED. (f) Comparison of ET for OSM.

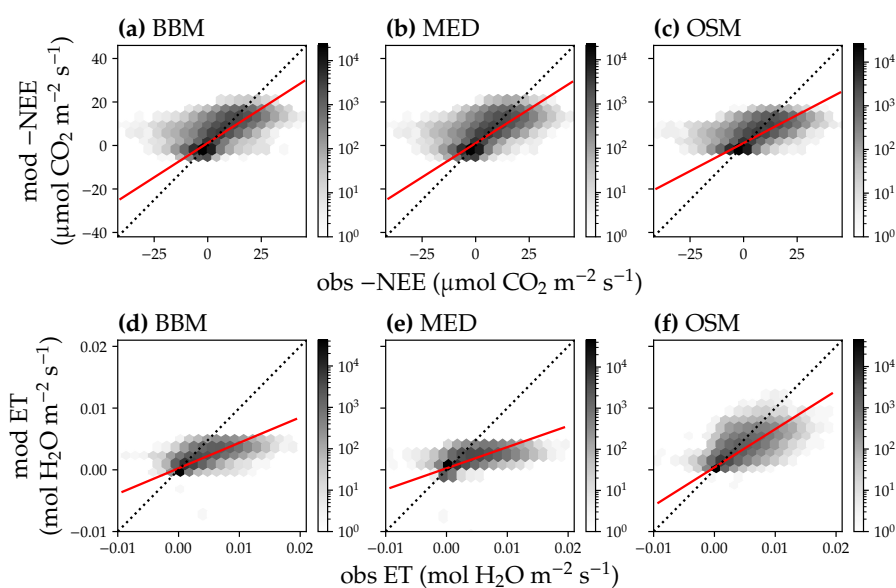


Figure 12. Comparison of half-hourly modeled and observed carbon and water fluxes for three stomatal models for US-MOz (MOFLUX, deciduous angiosperm forest) flux tower. (a) Comparison of modeled (y axis) and observed (x axis) net ecosystem carbon flux (NEE) for Ball et al. (1987) stomatal model (BBM). Shading represents density; the darker the hexagon, the more data that fell within the hexagon. The red solid line plots the linear regression of the data, and the black dotted line plots the 1:1 line. (b) Comparison of NEE for Medlyn et al. (2011) model (MED). (c) Comparison of NEE for Wang et al. (2020) model (OSM). (d) Comparison of ecosystem water flux (ET) for BBM. (e) Comparison of ET for MED. (f) Comparison of ET for OSM.



Sabot et al., 2020). Moreover, while the stomatal optimization model (Wang et al., 2020) had lower errors than the empirical models (Ball et al., 1987; Medlyn et al., 2011), the optimization model fitting parameters did not vary much (Figs. 9 and 10). In comparison, the empirical models required more variable parameterization among years to achieve a similar error (Figs. 9a and 10a). Furthermore, as the stomatal optimization model did not rely on empirical parameters like g_0 and g_1 , the stomatal optimization model can be used to simulate plant carbon and water fluxes with acclimated traits (Sperry et al., 2019). In comparison, it is unclear how g_0 and g_1 may vary with plant traits, adding extra uncertainties to modeling plant responses to future climate.

3.4.3 Land model parameterization

The empirical models using default CLM setups, in general, did not perform as well as the stomatal optimization model. This under-performance was probably related to (i) model parameterization, such as the g_1 we used may not be ideal for the two forest sites, and (ii) the use of a $V_{\text{cmax}25}$ tuning factor interfered the prescribed g_1 . For example, if the g_1 was meant to use with a tuning factor that affects g_1 itself rather than $V_{\text{cmax}25}$, then the use of g_1 with a $V_{\text{cmax}25}$ tuning factor would make the model more sensitive to air humidity when the plant suffers from a drought stress. The reason is that a $V_{\text{cmax}25}$ tuning factor would translate into changes in leaf water potential to changes in effective $V_{\text{cmax}25}$, and thus stomatal conductance decreases faster in response to drier air. In this case, the prescribed g_1 needs to be higher to mitigate the increased sensitivity resulted from the $V_{\text{cmax}25}$ tuning factor.

Indeed, when we fitted an extra g_1 for both BBM and MED models, we found improved predictive skills in tracking water flux as the slope between modeled and observed ET were closer to 1 (though still significantly lower than 1; Table 4; Figs. 13 and 14). However, the increase in the slopes of ET was accompanied with decreases in the slopes of NEE (Table 4; Figs. 13 and 14). As we expected, the fitted g_1 was much higher than in the CLM5 default setups (Table 3). The alteration of g_1 indeed shows potential in better capturing carbon and water fluxes than the tested stomatal optimization model (Table 4); and we believe more site-specific g_1 setups ought to improve the empirical model predictive skills. Yet, whether the fitted parameters also apply to other forests, and how to best represent the spatial and temporal variations of g_1 requires further investigation. Nevertheless, as g_1 is supposed to change with time, empirical model predicted future carbon and water fluxes may be of great uncertainty. In comparison, OSM was less dependent on empirical curve fitted parameters and had lower variation in the fitting parameters (Figs. 9 and 10), and thus the model predicted future carbon and water fluxes ought to be more reliable.

Our model simulations highlighted the importance of land model parameterizations, and the potential pitfalls for using unpaired or untested parameter sets in land surface modeling. Comparatively, the tested optimization model shows comparable predictive skills and it is less dependent on the empirical parameters (better than default CLM setups, worse than the scenario of fitting an extra g_1). Better future land model parameterization ought to improve the land surface modeling and thus Earth System modeling.

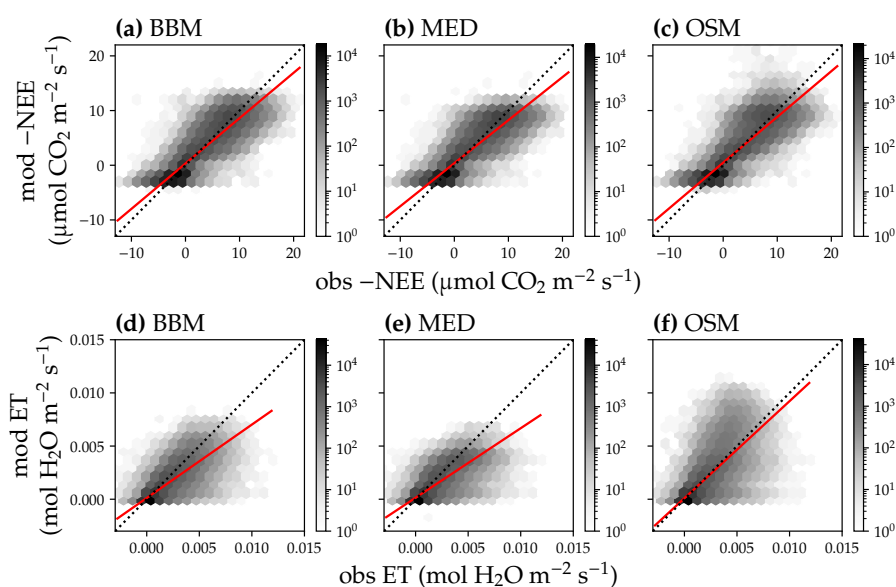


Figure 13. Comparison of modeled and observed carbon and water fluxes for three stomatal models when fitting an extra empirical model stomatal model parameter for US-NR1 (Niwo Ridge, evergreen gymnosperm forest) flux tower site. (a) Comparison of modeled (y axis) and observed (x axis) net ecosystem carbon flux (NEE) for Ball et al. (1987) stomatal model (labeled as BBM). The darker the hexagon is, the more data fall into the hexagon region. The red solid line plots the linear regression of the data, and the black dotted line plots the 1:1 line. (b) Comparison of NEE for Medlyn et al. (2011) model (labeled as MED). (c) Comparison of NEE for Wang et al. (2020) model (labeled as OSM). (d) Comparison of ecosystem water flux (ET) for BBM. (e) Comparison of ET for MED. (f) Comparison of ET for OSM. This figure differs from Fig. 11 in that g_{1s} (equations 4 and 5) for BBM and MED are also fitted.

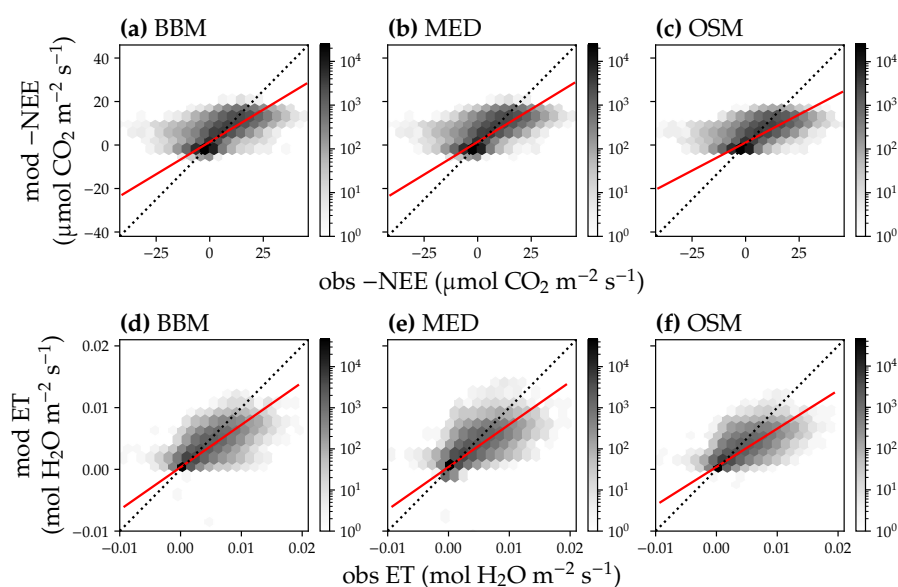


Figure 14. Comparison of modeled and observed carbon and water fluxes for three stomatal models when fitting an extra empirical model stomatal model parameter for US-MOz (MOFLUX, deciduous angiosperm forest) flux tower site. (a) Comparison of modeled (y axis) and observed (x axis) net ecosystem carbon flux (NEE) for Ball et al. (1987) stomatal model (labeled as BBM). Shading represents density; the darker the hexagon, the more data that fell within the hexagon. The red solid line plots the linear regression of the data, and the black dotted line plots the 1:1 line. (b) Comparison of NEE for Medlyn et al. (2011) model (labeled as MED). (c) Comparison of NEE for Wang et al. (2020) model (labeled as OSM). (d) Comparison of ecosystem water flux (ET) for BBM. (e) Comparison of ET for MED. (f) Comparison of ET for OSM. This figure differs from Fig. 12 in that g_{1s} (equations 4 and 5) for BBM and MED are also fitted.



4 Solar-induced chlorophyll fluorescence

4.1 Model simulations

We used the TROPOMI SIF retrievals that fell within the region of the flux tower sites to test our model, excluding retrievals
340 that had a cloud fraction higher than 10% (see Fig. 6 for the region map). For the gymnosperm site, we chose retrievals that had
at least 50% overlap with a representative area around the flux tower site (a total of 99 data points in year 2018 and 2019); for
the angiosperm site, we chose retrievals that had at least an 80% overlap with the representative site region (a total of 218 points
in year 2018 and 2019). For each valid TROPOMI SIF retrieval, we simulated the SIF emission using the actual sun-sensor
geometry angles with our ClIMA Land model (solar zenith angle, viewing zenith angle, and relative azimuth angle).

345 We first aligned the TROPOMI SIF retrievals with flux tower data (e.g., if the satellite observation occurred at 12:48 PM, we
aligned the data to a flux tower observation ranging from 12:30 PM to 13:00 PM). With the fitted $V_{\text{cmax}25}$, K_{max} , and R_{base} , we
calculated the photosynthetic rate and fluorescence quantum yield at each time step (van der Tol et al., 2014). We then used the
modeled quantum yield to simulate the canopy SIF spectrum for the given sun-sensor geometry. We modeled SIF at 740 nm
for both the gymnosperma and angiosperm forests for year 2018 and 2019, and compared our model simulated SIF₇₄₀ against
350 TROPOMI SIF₇₄₀. We simulated SIF in two scenarios: (i) a constant LAI (same prescribed value as the carbon and water flux
simulations) was used to simulate SIF throughout the year, and (ii) a time series of LAI from Moderate Resolution Imaging
Spectroradiometer (MODIS) were used (data from Yuan et al., 2011, spatial resolution: 1/20°, temporal resolution: 8 days).

4.2 Model performance

For both scenarios of LAI (using constant site LAI, or using variable MODIS LAI), modeled SIF well captured the trend of
355 TROPOMI SIF retrievals (Fig. 15, $P < 0.001$ for all four linear regressions). When using variable MODIS LAI, modeled
SIF had better agreement with the SIF retrievals (lower RMSE for both forests; Fig. 15). The statistically significant linear
correlation between modeled and observed SIF suggests that satellite-based remote sensing data has potential in constraining
future land model parameterization.

Our model captured the seasonal cycle of SIF compared to satellite observations, underscoring the potential to constrain
360 land model parameterization using remote sensing products. Yet, we were not able to obtain a one-to-one relationship between
modeled and retrieved SIF given the significant intercept ($P < 0.001$; Fig. 15). There are many potential reasons for the offset,
e.g. retrieval noise (some TROPOMI SIF values were lower than 0), mismatches in the spatial and temporal domain, inaccurate
parameters to model SIF (leaf biomass per area, leaf chlorophyll content, and seasonal changes in leaf area index), and high
sustained non-photochemical quenching (NPQ) at Niwot Ridge due to low temperature (accounting for the sustained NPQ
365 will make the modeled SIF lower in winter time, namely the points with lower observed SIF; Porcar-Castell, 2011; Raczka
et al., 2019). Despite all these imperfections, we still found a strong correlation between modeled and satellite-based SIF.
Further, when we used a time series of LAI (Yuan et al., 2011), the agreement between modeled and satellite-based SIF
increased, which indicated the potential of constraining land model parameters using remote sensing based results. Future

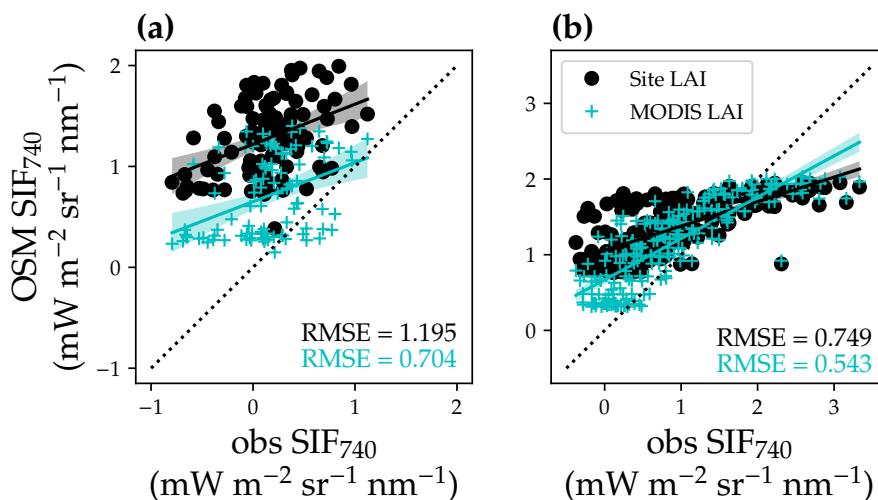


Figure 15. Comparison of modeled and satellite observed solar-induced chlorophyll fluorescence at 740 nm (SIF_{740}). **(a)** Comparison for the US-NR1 flux tower site (evergreen gymnosperm forest). The black circles plot the comparison with modeled SIF using a constant site LAI, and the cyan “+” plot that using a variable MODIS LAI time series. The black line with shaded confidence interval regions plots the linear regression for black circles ($y = 0.40x + 1.22, R^2 = 0.17, P < 0.001$). The cyan line with shaded regions plots the linear regression for cyan symbols ($y = 0.39 + 0.65, R^2 = 0.14, P < 0.001$). **(b)** Comparison for US-MOz flux tower site (deciduous angiosperm forest). The linear regressions are $y = 0.32x + 1.05, R^2 = 0.54, P < 0.001$ for black circles, and $y = 0.55x + 0.67, R^2 = 0.69, P < 0.001$ for cyan symbols.

research with improved parameterization of our land model and more accurate plant and site traits would likely improve the
370 model performance.

5 Conclusions

We implemented and tested a new land surface model that couples a comprehensive canopy radiative transfer scheme with a stomatal optimization model based on plant hydraulic traits, as well as two empirical stomatal models. We investigated how the three models performed at two flux tower sites (one dominated by gymnosperm species, and the other dominated by angiosperm
375 species). We compared model predicted carbon and water fluxes to flux tower estimations, and model predicted SIF to satellite-based TROPOMI SIF retrievals. All three stomatal models performed well in predicting site-level carbon fluxes, showing similar 1:1 correlations and errors among all three models. However, the stomatal optimization model showed better agreement with water flux observations, given the improved 1:1 comparison with the flux tower observation. In comparison, the empirical stomatal models underestimated water fluxes and had higher error, probably because of the non-ideal parameterization. Our
380 model also reproduced the seasonal pattern of canopy SIF, with dynamic ranges being different most likely due to heterogeneity in the area around the tower. We concluded that the representation of the land model using the stomatal optimization theory



385 along with a more comprehensive RT model has great potential in predicting site-level carbon and water fluxes. Furthermore, the use of a comprehensive RT scheme allows us to quantitatively and directly link land surface processes to remote sensing, making it possible to constrain land model parameterization with a broad range of remote sensing datasets. The rapidly growing regional and global datasets will make it easier to better parameterize and evaluate land surface modeling and better predict the future carbon cycle and climate.

Code and data availability. Flux tower dataset are freely available at AmeriFlux (registration required). The gridded MODIS LAI was available at <http://globalchange.bnu.edu.cn/research/laiv6>, and we also made available via “GriddingMachine.jl” (<https://github.com/CliMA/GriddingMachine.jl>). We refer the reader to the online documentation of “GriddingMachine.jl” for access of the datasets (along with other high quality gridded datasets such as TROPOMI SIF). We coded our model and did the analysis using Julia (version 1.6.0), and current version of the CliMA Land model is available from the project website: <https://github.com/CliMA/Land> under the Apache 2.0 License. The exact version of the model used to produce the results used in this paper is archived on Zenodo (Wang, 2021), as are input data and scripts to run the model and produce the plots for all the simulations presented in this paper (Wang, 2021).

Author contributions. YW designed and conducted the research. YW, CF, and RKB developed the CliMA Land model. PK performed the TROPOMI SIF retrieval. YW, PK, LH, RD, RKB, JDW, and CF performed the general data analysis and wrote the manuscript.

Competing interests. No competing interests

Acknowledgements. This research was made possible by Hopewell Fund and by the generosity of Eric and Wendy Schmidt by recommendation of the Schmidt Futures program. Part of this research was carried out at the Jet Propulsion Laboratory, California Institute of Technology, under a contract with the National Aeronautics and Space Administration (NASA). California Institute of Technology. Government sponsorship acknowledged. Copyright 2021. All rights reserved.



References

- Anav, A., Friedlingstein, P., Kidston, M., Bopp, L., Ciais, P., Cox, P., Jones, C., Jung, M., Myneni, R., and Zhu, Z.: Evaluating the land and ocean components of the global carbon cycle in the CMIP5 earth system models, *Journal of Climate*, 26, 6801–6843, 2013.
- Anderegg, W. R., Wolf, A., Arango-Velez, A., Choat, B., Chmura, D. J., Jansen, S., Kolb, T., Li, S., Meinzer, F. C., Pita, P., et al.: Woody plants optimise stomatal behaviour relative to hydraulic risk, *Ecology Letters*, 21, 968–977, 2018.
- Arora, V. K., Boer, G. J., Friedlingstein, P., Eby, M., Jones, C. D., Christian, J. R., Bonan, G., Bopp, L., Brovkin, V., Cadule, P., et al.: Carbon–concentration and carbon–climate feedbacks in CMIP5 earth system models, *Journal of Climate*, 26, 5289–5314, 2013.
- Badgley, G., Anderegg, L. D., Berry, J. A., and Field, C. B.: Terrestrial gross primary production: Using NIRV to scale from site to globe, *Global change biology*, 25, 3731–3740, 2019.
- Baldocchi, D., Falge, E., Gu, L., Olson, R., Hollinger, D., Running, S., Anthoni, P., Bernhofer, C., Davis, K., Evans, R., et al.: FLUXNET: A new tool to study the temporal and spatial variability of ecosystem-scale carbon dioxide, water vapor, and energy flux densities, *Bulletin of the American Meteorological Society*, 82, 2415–2434, 2001.
- Baldocchi, D. D.: How eddy covariance flux measurements have contributed to our understanding of Global Change Biology, *Global change biology*, 26, 242–260, 2020.
- Ball, J. T., Woodrow, I. E., and Berry, J. A.: A model predicting stomatal conductance and its contribution to the control of photosynthesis under different environmental conditions, in: *Progress in photosynthesis research*, pp. 221–224, Springer, 1987.
- Bowling, D. R., Logan, B. A., Hufkens, K., Aubrecht, D. M., Richardson, A. D., Burns, S. P., Anderegg, W. R., Blanken, P. D., and Eiriksson, D. P.: Limitations to winter and spring photosynthesis of a Rocky Mountain subalpine forest, *Agricultural and Forest Meteorology*, 252, 241–255, 2018.
- Braghiere, R. K., Quaife, T., Black, E., He, L., and Chen, J.: Underestimation of global photosynthesis in Earth System Models due to representation of vegetation structure, *Global Biogeochemical Cycles*, 33, 1358–1369, 2019.
- Braghiere, R. K., Quaife, T., Black, E., Ryu, Y., Chen, Q., De Kauwe, M. G., and Baldocchi, D.: Influence of sun zenith angle on canopy clumping and the resulting impacts on photosynthesis, *Agricultural and Forest Meteorology*, 291, 108065, 2020.
- Braghiere, R. K., Wang, Y., Doughty, R., Sousa, D., Magney, T. S., Widlowski, J.-L., Longo, M., Bloom, A. A., Worden, J., Gentine, P., and Frankenberg, C.: Accounting for canopy structure improves hyperspectral radiative transfer and sun-induced chlorophyll fluorescence representations in a new generation Earth System model, *Remote Sensing of Environment*, 2021.
- Campbell, G. S. and Norman, J. M.: *An introduction to environmental biophysics*, Springer Science & Business Media, 1998.
- Cowan, I. R. and Farquhar, G. D.: Stomatal function in relation to leaf metabolism and environment, *Symposia of the Society for Experimental Biology*, 31, 471–505, 1977.
- Dewar, R., Mauranen, A., Mäkelä, A., Hölttä, T., Medlyn, B., and Vesala, T.: New insights into the covariation of stomatal, mesophyll and hydraulic conductances from optimization models incorporating nonstomatal limitations to photosynthesis, *New Phytologist*, 217, 571–585, 2018.
- Eller, C. B., Rowland, L., Mencuccini, M., Rosas, T., Williams, K., Harper, A., Medlyn, B. E., Wagner, Y., Klein, T., Teodoro, G. S., et al.: Stomatal optimization based on xylem hydraulics (SOX) improves land surface model simulation of vegetation responses to climate, *New Phytologist*, 226, 1622–1637, 2020.
- Farquhar, G. D., von Caemmerer, S., and Berry, J. A.: A biochemical model of photosynthetic CO₂ assimilation in leaves of C₃ species, *Planta*, 149, 78–90, 1980.



- Frank, H. A. and Cogdell, R. J.: Carotenoids in photosynthesis, *Photochemistry and photobiology*, 63, 257–264, 1996.
- Frankenberg, C., Fisher, J. B., Worden, J., Badgley, G., Saatchi, S. S., Lee, J.-E., Toon, G. C., Butz, A., Jung, M., Kuze, A., et al.: New global
440 observations of the terrestrial carbon cycle from GOSAT: Patterns of plant fluorescence with gross primary productivity, *Geophysical
Research Letters*, 38, 2011.
- Friedlingstein, P., O’Sullivan, M., Jones, M. W., Andrew, R. M., Hauck, J., Olsen, A., Peters, G. P., Peters, W., Pongratz, J., Sitch, S., et al.:
Global carbon budget 2020, *Earth System Science Data*, 12, 3269–3340, 2020.
- Gu, L., Pallardy, S. G., Hosman, K. P., and Sun, Y.: Drought-influenced mortality of tree species with different predawn leaf water dynamics
445 in a decade-long study of a central US forest, *Biogeosciences*, 12, 2831–2845, 2015.
- Hartmann, H., Adams, H. D., Anderegg, W. R. L., Jansen, S., and Zeppel, M. J. B.: Research frontiers in drought-induced tree mortality:
Crossing scales and disciplines, *New Phytologist*, 205, 965–969, 2015.
- He, L., Chen, J. M., Pisek, J., Schaaf, C. B., and Strahler, A. H.: Global clumping index map derived from the MODIS BRDF product,
Remote Sensing of Environment, 119, 118–130, 2012.
- 450 IPCC: Climate change 2014: Synthesis report. Contribution of working groups I, II and III to the fifth assessment report of the Intergovern-
mental Panel on Climate Change, IPCC, Geneva, Switzerland, 2014.
- Jones, C., Robertson, E., Arora, V., Friedlingstein, P., Shevliakova, E., Bopp, L., Brovkin, V., Hajima, T., Kato, E., Kawamiya, M., and
Tjiputra, J.: Twenty-first-century compatible CO₂ emissions and airborne fraction simulated by CMIP5 earth system models under four
representative concentration pathways, *Journal of Climate*, 26, 4398–4413, 2013.
- 455 Jung, M., Schwalm, C., Migliavacca, M., Walther, S., Camps-Valls, G., Koirala, S., Anthoni, P., Besnard, S., Bodesheim, P., Carvalhais, N.,
et al.: Scaling carbon fluxes from eddy covariance sites to globe: synthesis and evaluation of the FLUXCOM approach, *Biogeosciences*,
17, 1343–1365, 2020.
- Kannenberg, S. A., Novick, K. A., and Phillips, R. P.: Anisohydric behavior linked to persistent hydraulic damage and delayed drought
recovery across seven North American tree species, *New Phytologist*, 222, 1862–1872, 2019.
- 460 Kennedy, D., Swenson, S., Oleson, K. W., Lawrence, D. M., Fisher, R., Lola da Costa, A. C., and Gentine, P.: Implementing plant hydraulics
in the community land model, version 5, *Journal of Advances in Modeling Earth Systems*, 11, 485–513, 2019.
- Kodis, G., Herrero, C., Palacios, R., Marino-Ochoa, E., Gould, S., De La Garza, L., Van Grondelle, R., Gust, D., Moore, T. A., Moore, A. L.,
et al.: Light harvesting and photoprotective functions of carotenoids in compact artificial photosynthetic antenna designs, *The Journal of
Physical Chemistry B*, 108, 414–425, 2004.
- 465 Köhler, P., Frankenberg, C., Magney, T. S., Guanter, L., Joiner, J., and Landgraf, J.: Global retrievals of solar-induced chlorophyll fluorescence
with TROPOMI: First results and intersensor comparison to OCO-2, *Geophysical Research Letters*, 45, 10,456–10,463, 2018.
- Koyama, Y., Rondonuwu, F. S., Fujii, R., and Watanabe, Y.: Light-harvesting function of carotenoids in photo-synthesis: The roles of the
newly found 11B state, *Biopolymers: Original Research on Biomolecules*, 74, 2–18, 2004.
- Lavigne, M. and Ryan, M.: Growth and maintenance respiration rates of aspen, black spruce and jack pine stems at northern and southern
470 BOREAS sites, *Tree Physiology*, 17, 543–551, 1997.
- Leuning, R.: A critical appraisal of a combined stomatal-photosynthesis model for C₃ plants, *Plant, Cell & Environment*, 18, 339–355, 1995.
- Medlyn, B. E., Duursma, R. A., Eamus, D., Ellsworth, D. S., Prentice, I. C., Barton, C. V. M., Crous, K. Y., de Angelis, P., Freeman, M.,
and Wingate, L.: Reconciling the optimal and empirical approaches to modelling stomatal conductance, *Global Change Biology*, 17,
2134–2144, 2011.



- 475 Mello, C. R. d., Oliveira, G. C. d., Ferreira, D. F., Lima, J. M. d., and Lopes, D.: Modelos para determinação dos parâmetros da equação de van Genuchten para um Cambissolo, *Revista brasileira de engenharia agrícola e ambiental*, 9, 23–29, 2005.
- Mencuccini, M., Manzoni, S., and Christoffersen, B.: Modelling water fluxes in plants: From tissues to biosphere, *New Phytologist*, 222, 1207–1222, 2019.
- Monson, R., Turnipseed, A., Sparks, J., Harley, P., Scott-Denton, L., Sparks, K., and Huxman, T.: Carbon sequestration in a high-elevation,
480 subalpine forest, *Global Change Biology*, 8, 459–478, 2002.
- Norby, R. J., Long, T. M., Hartz-Rubin, J. S., and O’neill, E. G.: Nitrogen resorption in senescing tree leaves in a warmer, CO₂-enriched atmosphere, *Plant and Soil*, 224, 15–29, 2000.
- Pinty, B., Lavergne, T., Dickinson, R., Widlowski, J.-L., Gobron, N., and Verstraete, M.: Simplifying the interaction of land surfaces with radiation for relating remote sensing products to climate models, *Journal of Geophysical Research: Atmospheres*, 111, 2006.
- 485 Porcar-Castell, A.: A high-resolution portrait of the annual dynamics of photochemical and non-photochemical quenching in needles of *Pinus sylvestris*, *Physiologia Plantarum*, 143, 139–153, 2011.
- Powell, T. L., Galbraith, D. R., Christoffersen, B. O., Harper, A., Imbuzeiro, H., Rowland, L., Almeida, S., Brando, P. M., Costa, A. C. L., Costa, M. H., and Moorcroft, P. R.: Confronting model predictions of carbon fluxes with measurements of Amazon forests subjected to experimental drought, *New Phytologist*, 200, 350–365, 2013.
- 490 Quéré, C. L., Andrew, R. M., Friedlingstein, P., Sitch, S., Pongratz, J., Manning, A. C., Korsbakken, J. I., Peters, G. P., Canadell, J. G., Jackson, R. B., et al.: Global carbon budget 2017, *Earth System Science Data*, 10, 405–448, 2018.
- Raczka, B., Porcar-Castell, A., Magney, T., Lee, J., Köhler, P., Frankenberg, C., Grossmann, K., Logan, B., Stutz, J., Blanken, P., et al.: Sustained nonphotochemical quenching shapes the seasonal pattern of solar-induced fluorescence at a high-elevation evergreen forest, *Journal of Geophysical Research: Biogeosciences*, 124, 2005–2020, 2019.
- 495 Rebbeck, J., Scherzer, A., and Gottschalk, K.: Do chestnut, northern red, and white oak germinant seedlings respond similarly to light treatments? II. Gas exchange and chlorophyll responses, *Canadian Journal of Forest Research*, 42, 1025–1037, 2012.
- Sabot, M. E., De Kauwe, M. G., Pitman, A. J., Medlyn, B. E., Verhoef, A., Ukkola, A. M., and Abramowitz, G.: Plant profit maximization improves predictions of European forest responses to drought, *New Phytologist*, 226, 1638–1655, 2020.
- Schimel, D., Pavlick, R., Fisher, J. B., Asner, G. P., Saatchi, S., Townsend, P., Miller, C., Frankenberg, C., Hibbard, K., and Cox, P.: Observing
500 terrestrial ecosystems and the carbon cycle from space, *Global Change Biology*, 21, 1762–1776, 2015.
- Schimel, D., Schneider, F. D., Carbon, J., and Participants, E.: Flux towers in the sky: global ecology from space, *New Phytologist*, 224, 570–584, 2019.
- Sperry, J. S. and Love, D. M.: What plant hydraulics can tell us about responses to climate-change droughts, *New Phytologist*, 207, 14–27, 2015.
- 505 Sperry, J. S. and Tyree, M. T.: Mechanism of water stress-induced xylem embolism, *Plant Physiology*, 88, 581–587, 1988.
- Sperry, J. S., Venturas, M. D., Anderegg, W. R. L., Mencuccini, M., Mackay, D. S., Wang, Y., and Love, D. M.: Predicting stomatal responses to the environment from the optimization of photosynthetic gain and hydraulic cost, *Plant, Cell & Environment*, 40, 816–830, 2017.
- Sperry, J. S., Venturas, M. D., Todd, H. N., Trugman, A. T., Anderegg, W. R. L., Wang, Y., and Tai, X.: The impact of rising CO₂ and acclimation on the response of US forests to global warming, *Proceedings of the National Academy of Sciences*, 116, 25 734–25 744,
510 2019.
- Sproull, G. J.: Long-term changes in four plant communities along an elevational gradient in the front range of Colorado, Ph.D. thesis, University of Denver, 2014.



- Sun, Y., Frankenberg, C., Jung, M., Joiner, J., Guanter, L., Köhler, P., and Magney, T.: Overview of Solar-Induced chlorophyll Fluorescence (SIF) from the Orbiting Carbon Observatory-2: Retrieval, cross-mission comparison, and global monitoring for GPP, *Remote Sensing of Environment*, 209, 808–823, 2018.
- 515 Environment, 209, 808–823, 2018.
- Tai, X., Mackay, D. S., Ewers, B. E., Parsekian, A. D., Beverly, D., Speckman, H., Brooks, P. D., and Anderegg, W. R.: Plant hydraulic stress explained tree mortality and tree size explained beetle attack in a mixed conifer forest, *Journal of Geophysical Research: Biogeosciences*, 124, 3555–3568, 2019.
- Trugman, A. T., Medvigy, D., Mankin, J. S., and Anderegg, W. R. L.: Soil moisture stress as a major driver of carbon cycle uncertainty, *Geophysical Research Letters*, 45, 6495–6503, 2018.
- 520 Geophysical Research Letters, 45, 6495–6503, 2018.
- van der Tol, C., Berry, J., Campbell, P., and Rascher, U.: Models of fluorescence and photosynthesis for interpreting measurements of solar-induced chlorophyll fluorescence, *Journal of Geophysical Research: Biogeosciences*, 119, 2312–2327, 2014.
- Venturas, M. D., Sperry, J. S., Love, D. M., Frehner, E. H., Allred, M. G., Wang, Y., and Anderegg, W. R. L.: A stomatal control model based on optimization of carbon gain versus hydraulic risk predicts aspen sapling responses to drought, *New Phytologist*, 220, 836–850, 2018.
- 525 Vilfan, N., Van der Tol, C., Muller, O., Rascher, U., and Verhoef, W.: Fluspect-B: A model for leaf fluorescence, reflectance and transmittance spectra, *Remote Sensing of Environment*, 186, 596–615, 2016.
- Wang, Y.: Test CliMA Land model with flux tower and TROPOMI SIF datasets, <https://doi.org/10.5281/zenodo.4762775>, 2021.
- Wang, Y., Sperry, J. S., Venturas, M. D., Trugman, A. T., Love, D. M., and Anderegg, W. R. L.: The stomatal response to rising CO₂ concentration and drought is predicted by a hydraulic trait-based optimization model, *Tree Physiology*, 39, 1416–1427, 2019.
- 530 Wang, Y., Sperry, J. S., Anderegg, W. R. L., Venturas, M. D., and Trugman, A. T.: A theoretical and empirical assessment of stomatal optimization modeling, *New Phytologist*, 227, 311–325, 2020.
- Wang, Y., Anderegg, W. R., Venturas, M. D., Trugman, A. T., Yu, K., and Frankenberg, C.: Optimization theory explains nighttime stomatal responses, *New Phytologist*, 230, 1550–1561, 2021.
- Wolf, A., Anderegg, W. R. L., and Pacala, S. W.: Optimal stomatal behavior with competition for water and risk of hydraulic impairment, *Proceedings of the National Academy of Sciences*, 113, E7222–E7230, 2016.
- 535 Proceedings of the National Academy of Sciences, 113, E7222–E7230, 2016.
- Wood, J., Sadler, E., Fox, N., Greer, S., Gu, L., Guinan, P., Lupo, A., Market, P., Rochette, S., Speck, A., et al.: Land-atmosphere responses to a total solar eclipse in three ecosystems with contrasting structure and physiology, *Journal of Geophysical Research: Atmospheres*, 124, 530–543, 2019.
- Yang, B., Hanson, P. J., Riggs, J. S., Pallardy, S. G., Heuer, M., Hosman, K. P., Meyers, T. P., Wullschleger, S. D., and Gu, L.-H.: Biases of CO₂ storage in eddy flux measurements in a forest pertinent to vertical configurations of a profile system and CO₂ density averaging, *Journal of Geophysical Research: Atmospheres*, 112, 2007.
- 540 Journal of Geophysical Research: Atmospheres, 112, 2007.
- Yang, P., Verhoef, W., and van der Tol, C.: The mSCOPE model: A simple adaptation to the SCOPE model to describe reflectance, fluorescence and photosynthesis of vertically heterogeneous canopies, *Remote sensing of environment*, 201, 1–11, 2017.
- Yuan, H., Dai, Y., Xiao, Z., Ji, D., and Shanguan, W.: Reprocessing the MODIS Leaf Area Index products for land surface and climate modelling, *Remote Sensing of Environment*, 115, 1171–1187, 2011.
- 545 Remote Sensing of Environment, 115, 1171–1187, 2011.
- Zarter, C. R., Adams III, W. W., Ebbert, V., Cuthbertson, D. J., Adamska, I., and Demmig-Adams, B.: Winter down-regulation of intrinsic photosynthetic capacity coupled with up-regulation of Elip-like proteins and persistent energy dissipation in a subalpine forest, *New Phytologist*, 172, 272–282, 2006.
- Zhou, S., Medlyn, B., Sabaté, S., Sperlich, D., and Prentice, I. C.: Short-term water stress impacts on stomatal, mesophyll and biochemical limitations to photosynthesis differ consistently among tree species from contrasting climates, *Tree Physiology*, 34, 1035–1046, 2014.
- 550 Tree Physiology, 34, 1035–1046, 2014.

<https://doi.org/10.5194/gmd-2021-154>
Preprint. Discussion started: 1 June 2021
© Author(s) 2021. CC BY 4.0 License.



Zhou, S., Medlyn, B. E., and Prentice, I. C.: Long-term water stress leads to acclimation of drought sensitivity of photosynthetic capacity in xeric but not riparian *Eucalyptus* species, *Annals of Botany*, 117, 133–144, 2016.